IMPLICIT CFD METHODS FOR FAST ANALYSIS OF ROTOR FLOWS

Mark Woodgate and George N. Barakos

CFD Laboratory, Department of Engineering
University of Liverpool, L69 3GH, U.K.
http://www.liv.ac.uk/flightscience/PROJECTS/CFD/ROTORCRAFT
Email: M.Woodgate@liverpool.ac.uk, G.Barakos@liverpool.ac.uk

Abstract

CFD based on the Navier-Stokes equations, is by far the most useful predictive method available today for helicopter analysis and design. The main drawback of CFD and perhaps the reason for it slow acceptance by design offices of helicopter manufacturers is apparently due to the substantial requirements of CPU time and the relatively slow turn-around times in comparison to lower-order methods. However, progress with CFD algorithms and parallel computing has allowed CFD analyses to be used more routinely. These include computations of aerofoil data that feed performance codes and analyses of rotors in hovering flight. The computation of unsteady flow cases is, however, still challenging. This paper presents alternative ways of tackling unsteady flow problems pertinent to rotorcraft using methods that aim to reduce the time-marching unsteady computations to more manageable steady-state solutions. The techniques investigated so far by the CFD laboratory of Liverpool include the time-linearised as well as the harmonic balance methods. The details of the methods are presented along with their implementation in the framework of the Helicopter Multi-Block CFD solver. Results were also obtained for several flow cases ranging from pitching/translating aerofoils to complete rotors. The results highlight the limitations of the time-linearised method and the potential of the harmonic balance. It was found that the time-linearised method can provide adequate results for cases where the unsteady flow is a rather small perturbation of a known mean. The harmonic balance method, proved to have larger range of applicability and provided adequate results for the analysis of unsteady flows. The required CPU time was reduced and the required core computer memory was increased. Overall, the harmonic balance method appears to be a possible alternative to time-marching CFD for a wide range of problems.

1 INTRODUCTION

Computational Fluid Dynamics is a predictive method that allows aerodynamicists to compare the performance of rotor designs and optimise these to fit a particular purpose. The use of CFD is now gaining momentum in the helicopter industry and several codes and examples have been presented in the open literature. At the University of Liverpool, the Helicopter Multi-Block (HMB) solver was developed specifically for the analysis of flows around helicopters and has been demonstrated for fundamental unsteady aerodynamic flows as well as flows around complete helicopter cases [1–4]. The results suggest that certain flows can be well-studied under a steady-state assumption and this allows for efficient CFD computations, parametric studies and repeated evaluations of designs with CFD. A good example of such a flow is the hovering helicopter rotor [5] that can be studied as a steady-state problem for a wide range of conditions. The analysis of unsteady flows is, however, harder and requires longer computations. Consequently, the number of designs that can be assessed within a given time frame is relatively small and the required computer resources also increase. In an ideal situation, one would like the ability to analyse rotors in forward flight without having to pay a high penalty in terms of required resources and turn-around time. For this reason, the CFD laboratory of Liverpool, embarked in a study of CFD methods that will tackle this problem and allow for unsteady flows to be investigated in an efficient fashion. This study is part of the UK REACT project aiming to look at active rotor technologies.

Following a literature survey, two main techniques were identified as possible candidates for this research. The first one is the use of time-linearised Navier-Stokes methods [6, 7] and the second one is an extension of the harmonic balance method [8–10]. Time linearised methods are used in turbomachinery and fixed-wing aircraft for the study of quasi-periodic flows like single-passage turbomachinery computations or for the generation of aircraft derivatives. The harmonic balance method is common in aeroelasticity but it is just emerging as a method for solving unsteady flows. Both methods have been implemented within the framework of the HMB solver and are assessed for a range of flow cases.

In this paper, the governing equations for the methods are first presented along with key points of their implementation in the HMB solver. Then, a set of test cases are selected for evaluation of the methods. The cases include the popular AGARD oscillating aerofoils [11], the coupled pitch-translation (dMdt computation) oscillation of aerofoils, as well as, the study of the ONERA two-bladed rotor in non-lifting forward flight [12]. Results are first presented for the time-linearised method and these are restricted to the study of the AGARD cases as well as simple wings. The method was found to be robust and efficient, although it is more suitable for cases with a well-identified mean flow. The harmonic balance method was then assessed for the Euler and URANS equations with very encouraging results.

2 THE HMB CFD SOLVER

2.1 *Time-marching methods*

The Helicopter Multi-Block (HMB) CFD code [4, 13–16] was employed for this work. HMB solves the unsteady Reynoldsaveraged Navier-Stokes equations on block-structured grids using a cell-centred finite-volume method for spatial discretisation. Implicit time integration is employed, and the resulting linear systems of equations are solved using a pre-conditioned Generalised Conjugate Gradient method. For unsteady simulations, an implicit dual-time stepping method is used, based on Jameson's pseudo-time integration approach [17]. The method has been validated for a wide range of aerospace applications and has demonstrated good accuracy and efficiency for very demanding rotor flows. For example, a detailed account of application to dynamic stall problems can be found in reference [2]. Several rotor trimming methods are available in HMB along with a blade-actuation algorithm that allows for the near-blade grid quality to be maintained on deforming meshes [14].

The HMB solver has a library of turbulence closures which includes several one- and two- equation turbulence models and even non-Boussinesq versions of the $k-\omega$ model. Turbulence simulation is also possible using either the Large-Eddy or the Detached-Eddy simulation approach. The solver was designed with parallel execution in mind and the MPI library along with a load-balancing algorithm are used to this end. For multi-block grid generation, the ICEM-CFD Hexa commercial meshing tool is used and CFD grids with 10-30 million points and thousands of blocks are commonly run with the HMB solver [3, 18].

Complete helicopter configurations use the sliding-mesh approach. The underlying idea, as well as, details of the implementation in HMB were previously described in Refs. [4,19]. The method can deal with an arbitrary number of sliding planes between meshes in relative motion. The main requirement is that the grid boundary surfaces of two meshes on either side of a sliding plane match exactly, while the mesh topology and meshes can be, and in general are, non-matching.

2.2 *Time-linearised method*

The idea behind the faster methods is to maintain the order of modelling currently used in the time-accurate computations of HMB but to reduce the considerable time required to calculate the solution. This is done by exploiting additional features in the flow solution. One such class of problems is where the flow is assumed to be fully developed and periodic in time, for example the flow past a rotor at design conditions. For a time-accurate calculation in might be necessary to step through a number of periods before a fully developed solution has been achieved however if periodicity is assumed it might be possible to avoid this.

The semi-discrete form of an arbitrary system of conservation laws in three spatial dimensions can be represented as

$$\frac{dW}{dt} = -R(W) \tag{1}$$

where

$$R(W) = \frac{\partial F(W)}{\partial x} + \frac{\partial G(W)}{\partial y} + \frac{\partial H(W)}{\partial z}, \tag{2}$$

W is the vector of conserved variables, and F, G and H are flux vectors.

There is an associated lose of generality and accuracy in using a linearised method. The assumption of linearity means that the results are only valid for small perturbations of the geometry and solution, any non linear effects of the flow that cause, for example, shifts in the frequency or modes will not be modelled.

However there is a body of evidence that indicates that linear Euler and Navier-Stokes calculations are adequate for a wide range of applications. These have predominantly been used in the investigation of the onset of flutter in turbomachinery [6, 7, 20, 21]. In these cases the damping of an arbitrarily small oscillation is of interest and so ideally suited for linearised methods.

Equation (1) is linearised by splitting the solution variable W into mean flow $\bar{W}$ and a perturbation flow $\tilde{W}$ parts

$$W = \bar{W} + \tilde{W}. \tag{3}$$

The magnitude of the perturbed flow is assumed to be much smaller than the magnitude of the mean flow. By substituting equation (3) into equation (1) gives

$$\begin{aligned}
&\frac{d\tilde{W}}{dt} \\
&+\frac{\partial}{\partial x}F(\bar{W}) + \frac{\partial}{\partial x}F(\bar{W},\tilde{W}) + \frac{\partial}{\partial x}F(\bar{W},\tilde{W}^{+}) \\
&+\frac{\partial}{\partial y}G(\bar{W}) + \frac{\partial}{\partial y}G(\bar{W},\tilde{W}) + \frac{\partial}{\partial y}G(\bar{W},\tilde{W}^{+}) \\
&+\frac{\partial}{\partial z}H(\bar{W}) + \frac{\partial}{\partial z}H(\bar{W},\tilde{W}) + \frac{\partial}{\partial z}H(\bar{W},\tilde{W}^{+}) \\
&= 0.
\end{aligned} \tag{4}$$

The components $F(\bar{W})$, $G(\bar{W})$ and $H(\bar{W})$ just depend on the mean flow solution $\bar{W}$. The components $F(\bar{W},\tilde{W})$, $G(\bar{W},\tilde{W})$ and $H(\bar{W},\tilde{W})$ depend on the mean flow solution $\bar{W}$ and terms which are first order perturbed flow variables $\tilde{W}$. In fact

$$\begin{aligned}
F(\bar{W},\tilde{W}) &= \bar{A}\tilde{W} \\
G(\bar{W},\tilde{W}) &= \bar{B}\tilde{W} \\
H(\bar{W},\tilde{W}) &= \bar{C}\tilde{W}
\end{aligned} \tag{5}$$

where A, B and C are the Jacobian matrices

$$A = \frac{\partial F}{\partial W}, \qquad B = \frac{\partial G}{\partial W}, \qquad C = \frac{\partial H}{\partial W}.$$

The components $F(\bar{W},\tilde{W}^{+})$, $G(\bar{W},\tilde{W}^{+})$ and $H(\bar{W},\tilde{W}^{+})$ depend on the mean flow solution $\bar{W}$ and terms which of at least second order in the perturbed flow variables $\tilde{W}$. These terms can be ignored given the assumption that the unsteadiness is small compared to the mean flow and hence the first order terms will dominate. This gives rise to the following two equations

$$\frac{\partial F(\bar{W})}{\partial x} + \frac{\partial G(\bar{W})}{\partial y} + \frac{\partial H(\bar{W})}{\partial z} = 0 \tag{6}$$

$$\frac{d\tilde{W}}{dt} + \frac{\partial(\bar{A}\tilde{W})}{\partial x} + \frac{\partial(\bar{B}\tilde{W})}{\partial y} + \frac{\partial(\bar{C}\tilde{W})}{\partial z} = 0. \tag{7}$$

The perturbed flow variables $\tilde{W}$ are then expanded in a Fourier series

$$\tilde{W}(t) = \sum_{k=-\infty}^{\infty} \hat{W}_k e^{ikt}. \tag{8}$$

where k is the frequency of the excitation. Substituting the Fourier series 8 into equation (7) and using the orthogonality of the modes gives

$$ik\hat{W}_k + \frac{\partial(\bar{A}\tilde{W}_k)}{\partial x} + \frac{\partial(\bar{B}\tilde{W}_k)}{\partial y} + \frac{\partial(\bar{C}\tilde{W}_k)}{\partial z} = 0 \quad \forall k. \quad (9)$$

The procedure is to first solve the mean flow equation (6). Then it is possible to solve for any k by using the mean flow solution $\bar{W}$ to calculate the Jacobian matrices $\bar{A}$, $\bar{B}$ and $\bar{C}$. Due to the linearity of equation (7) all the temporal modes are decoupled and can be calculated independently of each other. The cost is proportional to the number of temporal modes calculated. It should be noted for a real valued $\tilde{W}$ then $\hat{W}_{-k}$ is the complex conjugate of $\hat{W}_k$.

Hall and Clark [6] have shown that the use of strained co-ordinates improve the accuracy of a time linearised flow solver. The idea is that the computational mesh conforms to the motion of the blade. Hence the mesh is assumed to undergo small harmonic deformations about its steady position.

$$x(\xi,\eta,\zeta,\tau) = \xi + f(\xi,\eta,\zeta)e^{ik\tau} \quad (10)$$

$$y(\xi,\eta,\zeta,\tau) = \eta + g(\xi,\eta,\zeta)e^{ik\tau} \quad (11)$$

$$z(\xi,\eta,\zeta,\tau) = \zeta + h(\xi,\eta,\zeta)e^{ik\tau} \quad (12)$$

$$t(\xi,\eta,\zeta,\tau) = \tau \quad (13)$$

where f, g and h are the first-order amplitudes of grid motion about the mean positions ξ, η and ζ. Using both the motion of the computational coordinate system, and the unsteady flow field equation (3) up to first order terms, gives

$$W(\xi,\eta,\zeta,\tau) = \bar{W}(\xi,\eta,\zeta) + \tilde{W}(\xi,\eta,\zeta)e^{ik\tau}. \quad (14)$$

The mean flow $\bar{W}$ and the perturbation flow $\tilde{W}$ may be thought of as attached to the deforming computational grid. An observer in the fixed co-ordinate system (x,y,z) see unsteadiness in the flow due to both the unsteady perturbation in the variables $\tilde{W}$ and the deformation of the mean flow field $\bar{W}$. Substituting equations (10-14) into a flux vector F gives

$$F = \bar{F} + \frac{\partial\bar{F}}{\partial\bar{W}}\tilde{W}e^{i\omega\tau} + s\cdot\nabla\bar{F}e^{i\omega\tau} + \mathcal{F}e^{i\omega\tau} \quad (15)$$

where $\bar{F} = F(\bar{W},\xi,\eta,\zeta)$. Also

$$\nabla = \begin{pmatrix} \frac{\partial}{\partial\xi} \\ \frac{\partial}{\partial\eta} \\ \frac{\partial}{\partial\zeta} \end{pmatrix} \quad \text{and} \quad s = \begin{pmatrix} f \\ g \\ h \end{pmatrix}.$$

The first term on the right hand side of equation 15 represents the mean flux vector. The second term represents the fluctuations in the flux vector due to the perturbation flow $\tilde{W}$. The third term represents the fluctuations in the flux vector due to the perturbation in local of the computational cell. The last term represents the fluctuations in the flux vector due to the straining of the computational mesh. Because the mean solution is attached to the computational mesh straining the mesh coordinates induces stresses in the fluid.

It has been reported in [7] that simply freezing the turbulence model, that is using the value of eddy viscosity at the steady state solution $\bar{W}$ with no unsteady perturbation in the viscosity due to the unsteady perturbation flow $\tilde{W}$, produces physically incorrect solutions.

Regarding boundary conditions for wall-slip surfaces, the assumption is made that there is no flow through the surface. Suppose $\hat{P}$ is the position vector that describes the position of the surface and $\hat{n}$ is the surface unit normal then the non linear solid wall boundary condition is given by

$$\hat{V}\cdot\hat{n} - \frac{\partial\hat{P}}{\partial t}\cdot\hat{n} = 0$$

Expanding in a perturbation series and collecting terms of first order gives the linearised flow tangency condition

$$v\cdot n = -V\cdot n' + i\omega p\cdot n$$

where V and v are the mean flow and perturbation flow velocities respectively, n and n' are the mean and perturbation unit normals and p is the perturbation of the solid surface. Since the grid motion conforms to the motion of the solid surface then at the solid surface p is the same as the grid motion. The first term is the up-wash due to the surface motion. The second term is the up-wash due the translational velocity of the surface.

The no-slip equation is formed in the same way giving the equation

$$v = i\omega p.$$

The goal of the linearised solver is to approximate the effect of small, periodically unsteady perturbations of the geometry of a configuration on the flow field. The input consists of a mesh describing a geometry, an initial steady flow field on this mesh, the motion of the mesh and a single frequency. The output is then the complex Fourier coefficients at each point of the mesh which describe the amplitude and phase of the resulting flow perturbation.

The entire frequency domain calculation including the initial steady flow should be equivalent to the cost of 3 steady flow calculations. This should be contrasted with the effect required to perform a full unsteady analysis which might require anything from 100 to thousands flow computations depending on how fast the initial transient motion is damped.

The implementation currently in HMB is notationally different from that described above and is outlined below. Let the set of unsteady governing equations which are discretised in space with an arbitrary method be written

$$\frac{\mathrm{d}W}{\mathrm{d}t} + R(W,x,\dot{x}) = 0, \quad (16)$$

where R is termed the residual, and is a function of the flow solution W, the grid x and the grid velocities $\dot{x}$, all of which are functions of time t. The movement of the the grid, characterised by $x(t)$ is taken to be known and so (16) must be solved for $W(t)$.

Assuming the unsteady motion has a small amplitude and rewriting the unsteady terms as a sum of a steady mean solution plus an unsteady perturbation we write:

$$\begin{array}{rcll} W(t) &=& \bar{W} + \tilde{W}(t), & \|\tilde{W}\| \ll \|\bar{W}\| \\ x(t) &=& \bar{x} + \tilde{x}(t), & \|\tilde{x}\| \ll \|\bar{x}\| \\ \dot{x}(t) &=& \dot{\tilde{x}}(t). & \end{array}$$

The linearisation about the steady mean state results in the following two equations

$$R(\bar{W}, \bar{x}, 0) = 0, \tag{17}$$

and

$$\frac{\mathrm{d}\tilde{W}}{\mathrm{d}t} + \left.\frac{\partial R}{\partial W}\right|_{\bar{W},\bar{x}} \tilde{W} + \left.\frac{\partial R}{\partial x}\right|_{\bar{W},\bar{x}} \tilde{x} + \left.\frac{\partial R}{\partial \dot{x}}\right|_{\bar{W},\bar{x}} \dot{\tilde{x}} = 0 \tag{18}$$

Note that all derivatives of the residual are evaluated at $(\bar{W}, \bar{x}, 0)$. Equation (18) could be solved in the unsteady time-marching variant of the linearised equations but it does not represent a significant simplification in cost on the original non-linear system. In fact the evaluation of this of the linear residual currently is more expensive than that of the non-linear residual R.

As above the motion is assumed to be periodic and equation (18) becomes

$$\left[ik\omega I + \frac{\partial R}{\partial W}\right] \hat{W}_k = -\frac{\partial R}{\partial x}\hat{x}_k - ik\omega \frac{\partial R}{\partial \dot{x}}\hat{x}_k \tag{19}$$

The reason for using the above form over expanding the F of equation (2) in terms of equations (15) is that is clearer to see how the grid x terms contribute to the right hand side.

In HMB only the first order spatial scheme for the Euler equations as an analytic expression for the Jacobian $\partial R/\partial W$. All Navier-Stokes terms and higher order spatial schemes have approximations in them, hence currently all terms in equation (19) are approximated using finite differences.

$$\begin{aligned}
\frac{\partial R}{\partial W}\hat{W}_k &\approx \frac{R(\bar{W} + \epsilon W_k, \bar{x}, 0) - R(\bar{W} - \epsilon W_k, \bar{x}, 0)}{2\epsilon} \\
\frac{\partial R}{\partial x}\hat{x}_k &\approx \frac{R(\bar{W}+, \bar{x} + \epsilon\hat{x}_k, 0) - R(\bar{W}, \bar{x} - \epsilon\hat{x}_k, 0)}{2\epsilon} \\
\frac{\partial R}{\partial \dot{x}}\hat{x}_k &\approx \frac{R(\bar{W}+, \bar{x}, \epsilon\hat{x}_k) - R(\bar{W}, \bar{x}, -\epsilon\hat{x}_k)}{2\epsilon}
\end{aligned}$$

Equations (19) then have a pseudo-time term added and are advanced in pseudo time until steady state. It should be noted that if an exact Jacobian $\partial R/\partial W$ exists then equation (19) can be solved as a single complex linear solve at, however, 4 times the required storage. This is because the second order Navier-Stokes Jacobian matrix will have 34 non zero blocks pre row instead of 7 of the approximate Jacobian.

2.3 Harmonic balance method

Another alternative to time marching, the Harmonic Balance method allows for a direct calculation of the periodic state. It begins by writing the semi-discrete form as a system of ordinary differential equations:

$$I(t) = \frac{dW(t)}{dt} + R(t) = 0, \tag{20}$$

and assume the solution W and residual R to be periodic in time and functions of ω. Hence

$$W(t) = \hat{W}_0 + \sum_{n=1}^{\infty}\left(\hat{W}_{a_n}\cos(\omega n t) + \hat{W}_{b_n}\sin(\omega n t)\right) \tag{21}$$

$$R(t) = \hat{R}_0 + \sum_{n=1}^{\infty}\left(\hat{R}_{a_n}\cos(\omega n t) + \hat{R}_{b_n}\sin(\omega n t)\right) \tag{22}$$

It should be noted that for real Fourier coefficients and by using Euler's formula

$$\exp(ix) = \cos x + i\sin x$$

it is easy to express the real-valued function using either the complex form of the Fourier series or the trigonometric form, i.e.

$$a_n = c_n + c_{-n} \qquad b_n = i(c_n + c_{-n}) \qquad \forall n. \tag{23}$$

$$c_n = \frac{a_n - ib_n}{2} \qquad c_{-n} = \frac{a_n + ib_n}{2} \qquad \forall n. \tag{24}$$

Next the series is truncated to a specified number of harmonics N_H.

$$W(t) \approx \hat{W}_0 + \sum_{n=1}^{N_H}\left(\hat{W}_{a_n}\cos(\omega n t) + \hat{W}_{b_n}\sin(\omega n t)\right) \tag{25}$$

$$R(t) \approx \hat{R}_0 + \sum_{n=1}^{N_H}\left(\hat{R}_{a_n}\cos(\omega n t) + \hat{R}_{b_n}\sin(\omega n t)\right) \tag{26}$$

and equation 20 can also be truncated by a Fourier series expansion

$$I(t) \approx \hat{I}_0 + \sum_{n=1}^{N_H}\left(\hat{I}_{a_n}\cos(\omega n t) + \hat{I}_{b_n}\sin(\omega n t)\right). \tag{27}$$

A Fourier transform of equation 27 then yields

$$\begin{aligned}
\hat{I}_0 &= \frac{\omega}{2\pi}\int_0^{2\pi/\omega} I(t)\mathrm{d}t = \hat{R}_0, && (28)\\
\hat{I}_{a_n} &= \frac{\omega}{\pi}\int_0^{2\pi/\omega} I(t)\cos(\omega n t)\mathrm{d}t && (29)\\
&= \omega n\hat{W}_{b_n} + \hat{R}_{a_n}, \\
\hat{I}_{b_n} &= \frac{\omega}{\pi}\int_0^{2\pi/\omega} I(t)\sin(\omega n t)\mathrm{d}t && (30)\\
&= -\omega n\hat{W}_{a_n} + \hat{R}_{b_n}.
\end{aligned}$$

giving a system of equations for the Fourier series coefficients

$$\begin{aligned}
\hat{R}_0 &= 0 && (31)\\
\omega n\hat{W}_{b_n} + \hat{R}_{a_n} &= 0 && (32)\\
-\omega n\hat{W}_{a_n} + \hat{R}_{b_n} &= 0 && (33)
\end{aligned}$$

A system of $N_T = 2N_H + 1$ equations in N_T unknown harmonic terms and can be expressed as

$$\omega A\hat{W} + \hat{R} = 0 \tag{34}$$

where A is a $N_T \times N_T$ matrix containing the entries $A(n+1, N_H+n+1) = n$ and $A(N_H+n+1, n+1) = -n$, and

$$\hat{W} = \begin{pmatrix} \hat{W}_{a_0} \\ \hat{W}_{a_1} \\ \vdots \\ \hat{W}_{a_{N_H}} \\ \hat{W}_{b_1} \\ \vdots \\ \hat{W}_{b_{N_H}} \end{pmatrix} \qquad \hat{R} = \begin{pmatrix} \hat{R}_{a_0} \\ \hat{R}_{a_1} \\ \vdots \\ \hat{R}_{a_{N_H}} \\ \hat{R}_{b_1} \\ \vdots \\ \hat{R}_{b_{N_H}} \end{pmatrix} \tag{35}$$

The difficulty with solving equation 34 is in finding a relationship between $\hat{R}$ and $\hat{W}$. To avoid this problem the system is converted back to the time domain. The solution is split into N_T discrete equally spaced sub intervals over the period $T = 2\pi/\omega$

$$W_{hb} = \begin{pmatrix} W(t_0 + \Delta t) \\ W(t_0 + 2\Delta t) \\ \vdots \\ W(t_0 + T) \end{pmatrix}, \quad R_{hb} = \begin{pmatrix} R(t_0 + \Delta t) \\ R(t_0 + 2\Delta t) \\ \vdots \\ R(t_0 + T) \end{pmatrix} \tag{36}$$

where $\Delta t = 2\pi/(N_T\omega)$. Then there is a transformation matrix [9] E such that

$$\hat{W} = EW_{hb} \quad \text{and} \quad \hat{R} = ER_{hb}$$

and then equation 34 becomes

$$\begin{aligned} \omega AEW_{hb} + ER_{hb} = 0 = \\ \omega E^{-1}AEW_{hb} + E^{-1}ER_{hb} = \omega DW_{hb} + R_{hb} \end{aligned} \tag{37}$$

where $D = E^{-1}AE$ and the components of D are defined by

$$D_{i,j} = \frac{2}{N_T}\sum_{k=1}^{N_H} k\sin(2\pi k(j-i)/N_T)$$

Note that the diagonal $D_{i,i}$ is zero. We can then apply pseudo time marching to the harmonic balance equation

$$\frac{dW_{hb}}{dt} + \omega DW_{hb} + R_{hb} = 0 \tag{38}$$

This equation is solved using an implicit method, of which one step is written as

$$\frac{W_{hb}^{n+1} - W_{hb}^{n}}{\Delta t^*} = -\left[\omega DW_{hb} + R_{hb}(W_{hb}^{n+1})\right] \tag{39}$$

Considering one time solution of equation (39) and comparing it to the dual time stepping equation with $t^\star$the pseudo-time:

$$\frac{\partial \mathbf{W}_{i,j,k}^{n+1}}{\partial t^\star} + \frac{1}{V_{i,j,k}^{n+1}}\mathbf{R}_{i,j,k}^\star(\mathbf{W}^{n+1}) = 0 \tag{40}$$

it can be seen that the only difference is that the second order backward difference operator for the unsteady term has been replaced by a Fourier time operator which includes all the time steps in the cycle not just the last two. For a periodic solution which can be represented by a low number of modes this approximation is very accurate. In these cases it might be possible to replace the second order backward difference formulation of the unsteady residual with the Fourier decomposed formulation and get much faster convergence as the number of time-steps per cycle is increased. There are some drawbacks to this formulation of the unsteady residual. Firstly the whole last cycle is required to calculate the unsteady residual this is expensive in terms of storage and computational cost unless the number of time-steps per cycle is small. Secondly $D_{i,i} = 0$ makes the Jacobian less diagonally dominant than the backward difference case.

Returning to the system of equations for the harmonic balance system (38)

$$\frac{dW_{hb}}{dt} + \omega DW_{hb} + R_{hb} = 0, \tag{41}$$

the first method treats implicitly the residual R_{hb} but not the source term ωDW_{hb}

$$\frac{W_{hb}^{n+1} - W_{hb}^{n}}{\Delta t^*} = -\left[\omega DW_{hb}^{n} + R_{hb}(W_{hb}^{n+1})\right]. \tag{42}$$

This leads to the linear system

$$\begin{bmatrix} \left.\frac{\partial R}{\partial W}\right|_{t_0+\Delta t} & 0 & \cdots & 0 \\ 0 & \left.\frac{\partial R}{\partial W}\right|_{t_0+2\Delta t} & & \\ \vdots & & \ddots & \\ 0 & 0 & & \left.\frac{\partial R}{\partial W}\right|_{t_0+T} \end{bmatrix} \begin{bmatrix} \Delta W(t_0+\Delta t) \\ \Delta W(t_0+2\Delta t) \\ \vdots \\ \Delta W(t_0+T) \end{bmatrix} = -\begin{bmatrix} R(t_0+\Delta t) + \omega D_{1,j}W_{hb} \\ R(t_0+2\Delta t) + \omega D_{2,j}W_{hb} \\ \vdots \\ R(t_0+T) + \omega D_{N_T,j}W_{hb} \end{bmatrix}. \tag{43}$$

The right hand side is just the standard residual operator calculated at the ith snapshot plus the Fourier approximation of the unsteady residual. The left hand side is just the standard Jacobian operator calculated at the ith snapshot. The matrix is block diagonal and can be solved independently for each of the N_T instances. Hence N_T steady flows are computed and they are only coupled through the Fourier approximation of the unsteady residual. This method has one very clear advantage in that only the ith snapshot of the Jacobian has to be stored at once so not extra memory is required for the linear solver over the standard method. However the explicit treatment of the source term is likely to restrict the size of the CFL number and this problem increases with the number of modes used.

In order to increase the size of the usable CFL number and allow for more modes, an implicit treatment of the source term needs to be used.

$$\omega DW_{hb}^{n+1} = \omega DW_{hb}^{n} + \omega D(\Delta W_{hb}). \tag{44}$$

The unsteady term couples together the variables at all N_T snapshots which leads to a coupling of the increments also, and the equation (38) becomes

$$\frac{W_{hb}^{n+1} - W_{hb}^{n}}{\Delta t^*} = -\left[\omega DW_{hb}^{n+1} + R_{hb}(W_{hb}^{n+1})\right] \tag{45}$$

Hence the Jacobian matrix J is

$$J = \begin{bmatrix} \left.\frac{\partial R}{\partial W}\right|_{t_0+\Delta t} & \omega D_{1,2} & \dots & \omega D_{1,N_T} \\ \omega D_{2,1} & \left.\frac{\partial R}{\partial W}\right|_{t_0+2\Delta t} & & \\ \vdots & & \ddots & \\ \omega D_{N_T,1} & \omega D_{N_T,2} & & \left.\frac{\partial R}{\partial W}\right|_{t_0+T} \end{bmatrix} \tag{46}$$

and the linear system that needs to be solved is

$$\left[\frac{V}{\Delta t^\star} + J\right] \Delta W_{hb} = -R^n_{hb} - \omega D W^n_{hb} \tag{47}$$

where $\partial R/\partial W$ is the Jacobian matrix of the CFD residual. There are two considerations when solving equation (47). First, for solving the CFD systems it is normally more efficient, CPU time wise, to use an approximate Jacobian matrix based on a lower-order spatial discretisation of the residual function. This results in a linear system that has less terms in the coefficient matrix and is better conditioned due to be more diagonal dominant. Second a sparse matrix solver is used to calculate the updates from the solution of the linear system. The key issue is normally in the pre-conditioning used, and block incomplete lower upper (BILU) factorisation has proved effective for systems arising from CFD systems.

For solving the harmonic balance system several experiments were made based on experience with solving for a CFD steady state. First, for the terms on the diagonal of J, arising from the CFD residual, an approximate Jacobian matrix arising from the first-order discretisation of R is used. The linear system is solved using a Krylov subspace method with BILU factorisation with no fill-in.

The main drawback of this fully implicit method is that the memory requirements increase faster than $2N_H + 1$ times the steady state solver requirements. This is due to the extra memory needed to store the off block diagonals in the pre-conditioner. To try and lessen this requirement a Block Jacobi Strategy will now be considered.

Sicot *et al.* [22] proposed a Block-Jacobi symmetric-over-relaxation treatment of the source term which allows the implicit coupling obtained in the unsteady term is moved to the right hand side hence yielding $2N_H + 1$ independent linear systems as in the explicit scheme. Let

$$J_i = \left.\frac{\partial R}{\partial W}\right|_{t_0+i\Delta t} \tag{48}$$

be the Jacobian of the ith snapshot then the Jacobi step l is

$$\left[\frac{V}{\Delta t^\star} + J_i\right] \Delta W_i^{l+1} = -R^n_i - \omega D W^n_i - \omega D(\Delta W^l_i), \quad 1 \le i \le N_T \tag{49}$$

with $l \ge 0$, and $\Delta W^0_i = 0$. After l_{max} iterations:-

$$W_i^{n+1} = W_i^n + \Delta W_i^{l_{max}} \tag{50}$$

For each block Jacobi step a linear system has to be solved and this can be done with the “normal” steady state method.

3 Test Cases - Linearised method

3.1 *The Complex Variable Linear System*

The new solver takes a real Jacobian matrix A, an integer k, real ω and a complex residual b as the right hand side to solves the system

$$(A - i\omega k)x_k = b.$$

The complex variable pre-conditioner has been tested by using complete fill-in so the pre-conditioner becomes the inverse of A. Complex right hand sides have been constructed for different values of ω and k and random complex right hand sides. It was found for small values of ωk it is possible to construct the pre-conditioner by dropping all the complex terms - and hence saving memory - and still have good convergence rate. However for values larger than 0.2 in these simple tests the linear solver would fail to converge if they were not included. The number of iterations required to converge was about 50% more than the system with $\omega k = 0$.

3.2 *Pitching Aerofoils*

A periodic motion of the aerofoil is defined by the angle of attack as a function of time such that

$$\alpha(t) = \alpha_m + \alpha_0 \sin(\omega t)$$

where ω is related to the reduced frequency k by

$$k = \frac{\omega c}{2U_\infty}.$$

The first test case has a free-stream Mach number of 0.5, a mean incidence $\alpha_m = 0.0$, a reduced frequency $k = 0.1$, and small amplitude of oscillation of $\alpha_0 = \{0.5, 1.0, 2.0, 4.0, 8.0\}$ about the quarter chord.

Considering the leading and trailing edge points (x_1, x_2) of an aerofoil pitching about $x/c = 0.25$, at $t = 0$ the distance in the x-direction is maximal. As the aerofoil pitches up this distance shrinks to a minimum value at $t = \pi/(2\omega)$. The distance then recovers as the aerofoil returns to zero angle of attack. So even though the motion of the aerofoil has a sinusoidal motion of period $2\pi/\omega$, points in the grid move with frequency π/ω and so both x_1 and x_2 will have non zero terms.

From the above description of the motion for the aerofoil it is clear that the chord of the mean grid is smaller than the chord of the original aerofoil. The chord of the mean grid is

$$\frac{1 + \cos\alpha_0}{2} \approx 1 - \frac{\alpha_0^2}{4} + \frac{\alpha_0^4}{48}$$

Because the amplitude of the oscillation is small the differences in the mean grid $\bar{x}$ is very minor as can be seen from Figure 1. Even with $\alpha_0 = 8.0$ the chord has been reduced by only 0.5% which makes the difference between the steady solution W on the steady grid and the mean solution $\bar{W}$ on the mean grid nearly identical.

Next consider how x_1 and x_2 behave as the amplitude of the oscillation is increased. For a sinusoidal motion $\Re x_1 = 0$, the imaginary part $\Im x_1$ is directly proportional to the amplitude of the oscillation, $\Im x_2 = 0$ and the real part $\Re x_2$ is directly proportional to the square of amplitude of the oscillation. This very small change in the grid implies a very small change in the solution of $R(\bar{W}, \bar{x}, 0) = 0$ in fact to the accuracy of a steady state solve the same $\bar{W}$ can be used in all five different values of α_0 of this test case. For linearised method to give a good representation of the nonlinear solution method two comparisons can be applied. Firstly the mean solution $\bar{W}$ from equation (17) should compare well to the average of the non linear solution and secondly it is possible to compare the $\hat{W}_k$ form equation (19) with a Fourier decomposition of the non linear solution. Figures 2 and 3 show how the average of a cycle of the non linear system behaves. The figures present the obtained results for all five amplitudes of oscillation for the first and second order spatial schemes. The results are in fair agreement with each other. The case of 8 degrees of amplitude is clearly different.

One possibility of improving the solution is replacing the mean solution at a given angle with the non linear mean. Take a Fourier series of a point P such that

$$P(t) = a_0 + \sum_{n=1}^{\infty} \left(a_n \cos(\omega n t) + b_n \sin(\omega n t)\right). \qquad (51)$$

Consider the curve shown in figure 4 which has $a_n = b_n = 0$, $\forall n > 1$. The mean solution is a_0 and consider two times t_1 and t_2 such that

$$\sin(\omega t_1) = \sin(\omega t_2 \quad \text{hence} \quad \cos(\omega t_1) = -\cos(\omega t_2)$$

then the average of the solution is

$$\frac{1}{2}\left(P(t_1) + P(t_2)\right) = a_0 + b_1 \sin(\omega t_1).$$

If this is then replaced with a new solution $P^{\star}(t_1)$ then the mean solution is the $P^{\star}(t_1) - b_1 \sin(\omega t_1)$. Consider the case at $t_1 = 0$ then the mean solution is replaced by the steady state solution at zero angle of attack, which as shown above is a very good approximation to the solution of mean equation (17) and hence has not improved the solution. The other extrema, where $t_1 = \pi/(2\omega)$, is considered in figure 8 for the ± 8 degree case described above. As can be seen the the steady solutions show a large variation of pressure around the leading edge. It seems clear that at the end points ± 8 degrees the replacement mean will only be a good approximation to the unsteady solution at very low values of the reduced frequency.

Figures 5 and 6 present raw and scaled results for the real and imaginary components of the obtained pressure for the oscillating aerofoil case using first and second order spatial schemes. It is evident that the obtained approximations of this unsteady flow are not poor with the exception of the 8 degree case that shows small deviations from the rest. The same information is plotted in figure 7 as a function of the cell index around the aerofoil instead of the chord. This way the differences between the obtained solutions are more visible. The obtained flow-field from the steady-state and the linearised unsteady methods are compared in Figure 8.

To gradually build the complexity of the test cases, several computations were performed for the well-known AGARD [11] cases. The first test case had a free-stream Mach number of 0.5, a mean incidence $\alpha_m = 0.0$, a reduced frequency $k = 0.1$, and a small amplitude of oscillation of $\alpha_0 = 4.0$ about the quarter chord. This was followed by the CT1, CT2, CT3 and CT5 cases. This last AGARD test case, CT5, has a free-stream Mach number of 0.755, a mean incidence $\alpha_m = 0.016$ degrees, a reduced frequency $k = 0.0814$, and small amplitude of oscillation of $\alpha_0 = 2.51$ degrees about the quarter chord. The obtained results from these computations are shown in Figures 10, 11, 12 and 13. For all cases where the mean flow is contains the key features of the instaneous flows, the linearized method worked well. Discrepencies are present for cases where the mean flow did not includ, for example, shocks and therefore the instaneous linearized solutions were different from the time-marching.

3.3 *Harmonic Translation of an Aerofoil at Fixed Angle of Attack*

To increase the complexity of the cases and include some variation of the Mach number the harmonic translation (dMdt case) of an aerofoil was also considered. If the angle of attack is fixed then there is no change in the y co-ordinates and in this case the stream-wise velocity U is changed sinusoidally so that

$$U = U_{\text{ref}} + \mu sin(\omega t). \qquad (52)$$

This change in stream-wise velocity is obtained thought the use of grid velocities by moving the x coordinates using

$$x = x - \mu cos(\omega t)/\omega \qquad (53)$$

The mean grid $\bar{x}$ in this case is just the original grid translated to the left by $\mu/(2\omega)$ with no other deformations. Hence the mean solution $\bar{W}$ is independent of both μ and ω and is just the steady state solution at the given angle of attack. From this fact it is clear that the method may encounter difficulties since the non linear unsteady flow solutions will scale very differently as the advancing side becomes transonic. The results shown in Figure 14 confirm this since these do not appear to match the time-marching method.

The complete pressure field has been reconstructed for the CT cases and the dMdt case at a point $48/128$ into the cycle. The Results can be seen in Figure 15. The coloured contours represent the time-marching values while the solid black lines correspond to the linearised solution.

3.4 *Viscous and 3D Cases*

A viscous, laminar test case was also computed at a free-stream Mach number of 0.5, a mean incidence i $\alpha_m = 0.0$, a reduced frequency $k = 0.1$, and small amplitude of oscillation of $\alpha_0 = 0.5$ about the quarter chord. The results shown in Figure 16 confirm the good agreement of the time-marching and linearised methods for this test case. The results of the reconstruction for the viscous flow test case can be seen in Figure 17 and this confirms that treatment of the viscous terms is not a problem with this method. Further, an Euler 3D wing test case was also computed. This one was based on the AGARD M6 Wing at a free-stream Mach number of 0.84, a mean incidence $\alpha_m = 3.06$, a reduced frequency $k = 0.1$, and small amplitude of oscillation of $\alpha_0 = 0.5$ about the quarter chord. Results for this test case are shown in Figure 18.

3.5 Timings of the Linearised Method

The exact Jacobian is required to solve equation 19 with a single iteration - making the calculating linearised part 10 times faster than even a steady state solve. In general this is not the case and equation 19 is solved in pseudo-time. As is shown in figure 19 there are 2 additional steps after solving the original steady state problem. Firstly equation 17 is solved which only requires a few iterations because the steady solution on the original grid is an excellent starting solution for the steady solution on the mean grid. The second part is the solution of equation 19 which takes a similar number of iterations to the original steady state problem. This can be explained as the second order spatial Jacobians are very similar and approximated in exactly the same way. So the linearised method takes less than 3 steady state solves while the non linear time marching method takes 100+ steady state solves leading to at least a factor of 30 improvement.

4 TEST CASES - HARMONIC BALANCE

When comparing the computation cost of a N_H mode harmonic balance method with the unsteady solver two main scalings appear and are shown in table 1. Firstly $2N_H + 1$, since this is how many snapshots, scales the calculation of the Residual, Jacobian and the vector operations in the linear solver. However for the fully coupled implicit scheme there is also a $2N_H + 1 + 2N_H(2N_H + 1)/7$ scaling. The second term is the contributions of the unsteady source term - which is treated implicitly. This term appears only on the diagonal and hence divided through by the average non zero blocks per row. This scaling effects the sparse matrix vector multiplications all operation on the pre-conditioner.

To calculate a rough estimate on the computational cost consider an unsteady forward flying rotor which takes 4 complete cycles with 0.25 degree updates each unsteady step with 100 inner iterations per unsteady step. This leads to $576,000$ linear system solves. It is possible to work out the approximate cost of each inner iteration of the N_H mode harmonic balance method with a couple of approximations. Firstly by profiling the unsteady code the split between the 2 difference scaling is approximately 40% of the vector scaling and 60% for the matrix scaling. Now the linear system will be harder to solve as more off diagonal blocks have been added to the Jacobian so assuming it takes twice the number of iterations then table 2 can be calculated.

To assess the performance of this method, the combined pitch-translation oscillation was used. For this case, the incidence and Mach number of the aerofoil were changing at the same time in an attempt to mimic the conditions around a rotor blade. The time-marching solution was first obtained and it is shown in Figure 20 as black solid lines. The initial solution for the computations shown in this paragraph is compared with the time-marching solution in the same figure. The initial solution was simply the steady-state flow at the instantaneous Reynolds and Mach number and at the same incidence and grid speeds as the time-marching solution at each azimuth.

Inviscid results for this case are shown in Figure 21 for the lift, moment and drag coefficients around the azimuth. Solutions of several modes have been obtained using the implicit and explicit formulations. The results show that the solution with 5 modes is close to the experimental data and it is an overall satisfactory approximation to the time-marching results around the azimuth. A further increase of the modes to 13 was also attempted and results are shown in Figure 22. The solution matches very well the drag and moment coefficients at all positions around the azimuth. A viscous, turbulent solution using the $k - \omega$ model was also attempted and the results with 5 modes are shown in Figure 23. This is a very encouraging result suggesting that the current method can be used to re-construct accurate loads for this case. The complexity of the turbulent flow did not influence the convergence of the method. Further computations shown in Figure 24 with 7 modes suggest an even better prediction and the convergence plot for the drag coefficient of each of the modes is also shown. The solution appears to be converged after just about 700 iterations.

Flow-field reconstructions for the dMdt inviscid and viscous cases can be seen in Figures 25 and 26, respectively. The coloured contours represent the time-marching solution that is very closely matched by the harmonic balance method represented by the black solid lines.

A final test case attempted was the forward-flying two-bladed, non-lifting ONERA rotor. The obtained results are shown in Figure 27. The overall flow-field compares very well and the harmonic balance method captured the strong shocks present in this flow. Looking at the comparison of the surface pressure coefficients, one has see that the harmonic balance and the time-marching methods differ in the strength of the shock at azimuth angles of 144 degrees. This is apparently due to the low number of modes employed for this complex case. This flow has strong shock hysteresis that may need more modes to be fully resolved.

5 CONCLUSIONS

The HMB solver has been extended to include time-linearised and harmonic balance methods. The implementation of the linearised method resulted in a robust technique with low memory requirements and substantial time benefits for the case where a well-identified mean flow is available. This method was adequate for computing oscillating aerofoils with small oscillation amplitude and captured some of the characteristics of the dMdt cases. The method is, however, limited and although very efficient it can be used for a relatively small number of problems within the helicopter CFD domain. The harmonic balance method was found to be robust and efficient in terms of the required CPU time. On the other hand, the method required more core memory than time-marching CFD. The results for a range of test cases were more than encouraging, suggesting that this method is a realistic alternative to time-marching CFD for several rotor cases including compete rotors in forward flight. Across the board the method delivered results of high fidelity matching very closely the time marching solutions. The implementation of the method results in an enhanced HMB solver although the memory requirements of the current implementation does not scales linearly with the number of flow modes requested. Due to the success of this method, further computations are to be undertaken to establish its envelope of applicability and its accuracy. The current results suggest that this method will be of high value for design studies providing accurate results for forward-flying rotor cases with reasonable turn-around times.

Acknowledgements
The financial support through the REACT programme of AgustaWestland and the DBERR of UK is gratefully acknowledged.

REFERENCES

[1] R. Morvant, K.J. Badcock, G.N. Barakos, and B.E. Richards. Aerofoil-Vortex Interaction Using the Compressible Vorticity Confinement Method. *AIAA J.*, 43(1):63–75, 2004.

[2] A. Spentzos, G. Barakos, K. Badcock, B.E. Richards, P. Wernert, S. Schreck, and M. Raffel. CFD Investigation of 2D and 3D Dynamic Stall. *AIAA J.*, 34(5):1023–1033, 2005.

[3] O. Boelens, G. Barakos, M. Biava, A. Brocklehurst, M. Costes, A. D'Alascio, M. Dietz, D. Drikakis, J. Ekatarinaris, I. Humby, W. Khier, B. Knutzen, F. Le Chuiton, K. Pahlke, T. Renaud, T. Schwarz, R. Steijl, L. Sudre, L. Vigevano, and B. Zhong. The Blind-Test Activity of the GOAHEAD Project. 33rd European Rotorcraft Forum, Kazan, Russia, September, 2007.

[4] R. Steijl and G.N. Barakos. Sliding Mesh Algorithm for CFD Analysis of Helicopter Rotor-Fuselage Aerodynamics. *Int. J. Numer. Meth. Fluids*, 58:527–549, 2008.

[5] A. Brocklehurst, R. Steijl, and G. Barakos. Developing Insights using CFD-Tail Rotor CFD Analysis and Design. 33th European Rotorcraft Forum, Kazan, Russia, 11-13 September, 2007.

[6] K. C. Hall and W. S. Clark. Linearized Euler predictions of unsteady aerodynamic loads in cascades. *AIAA Journal*, 31(3):540–550, 1993.

[7] W. S. Clark and K. C. Hall. A time-linearized Navier-Stokes analysis of stall flutter. *Journal of Turbomachinery*, 122(3):467–476, 2000.

[8] K. C. Hall, J. P. Thomas, and W. S. Clark. Computation of unsteady nonlinear flows in cascades using a harmonic balance technique. *AIAA Journal*, 40(5):879–886, 2002.

[9] J. P. Thomas, E. H. Dowell, K. C. Hall, and C. M. Denegri. Further investigation of modeling limit cycle oscillation behaviour of the F-16 fighter using a harmonic balance approach. In *AIAA Paper 2005-1917*, Austin, TX, April 2005. 46th AIAA/ASME/ASCE/AHS/ASC Structures, Structural Dynamics and Materials (SDM) conference.

[10] M. A. Woodgate and K. J. Badcock. Implicit harmonic balance solver for forced motion transonic flow. *AIAA Journal*, 47(4):893–901, 2009.

[11] R.H. Landon. NACA0012 oscillatory and transient pitching, compendium of unsteady aerodynamic measurements. Technical Report 702, AGARD, January 1982.

[12] J-J Philippe and J-J Chattot. Experimental and theoretical studies on helicopter blade tips at ONERA. Sixth European Rotorcraft and Powered Lift Aircraft Forum, Bristol, September 16-19, 1980.

[13] G. Barakos, R. Steijl, K. Badcock, and A. Brocklehurst. Development of CFD Capability for Full Helicopter Engineering Analysis. 31st European Rotorcraft Forum, 13-15 September 2005, Florence, Italy, 2005.

[14] R. Steijl, G.N. Barakos, and K.J. Badcock. A Framework for CFD Analysis of Helicopter Rotors in Hover and Forward Flight. *Int. J. Numer. Meth. Fluids*, 51:819–847, 2006.

[15] R. Steijl, M. Woodgate, and G. Barakos. CFD requirements for efficient smart-rotor analysis. 35th European Rotorcraft Forum, Hamburg, Germany, 22-25 September, 2009.

[16] G. Barakos, R. Steijl, and M. Woodgate. Towards CFD analysis of complete helicopter configurations. 3rd International Basic Research Conference on Rotorcraft Technologies, Nanjing, China, 14-16 October, 2009.

[17] A. Jameson. Time Dependent Calculations Using Multigrid, with Applications to Unsteady Flows past Airfoils and Wings. AIAA Paper 1991-1596, 10th Computational Fluid Dynamics Conference , Honolulu, Hawai, June 24-26, 1991.

[18] R. Steijl and G.N. Barakos. A Computational Study of the Advancing Side Lift Phase Problem. *Journal of Aircraft*, 45(1):246–257, 2008.

[19] R. Steijl and G.N. Barakos. Computational Study of Helicopter Rotor-Fuselage Aerodynamic Interactions. *AIAA Journal*, 47(9):2143–2157, 2009.

[20] K.C. Hall, W.S. Clark, and C.B. Lorence. A linearized Euler analysis of unsteady transonic flows in turbomachinery. *Journal of Turbomachinery*, 116(3):477–488, 1994.

[21] D. Hoyniak and W.S. Clark. Aerodynamic damping predictions using a linearized Navier-Stokes analysis. In *ASME Paper 99-GT-207*, 1999.

[22] F. Sicot, G. Puigt, and M. Montagnac. Block-jacobi implicit algorithms for the time spectral method. *AIAA Journal*, 46(12):3080–3089, 2009.

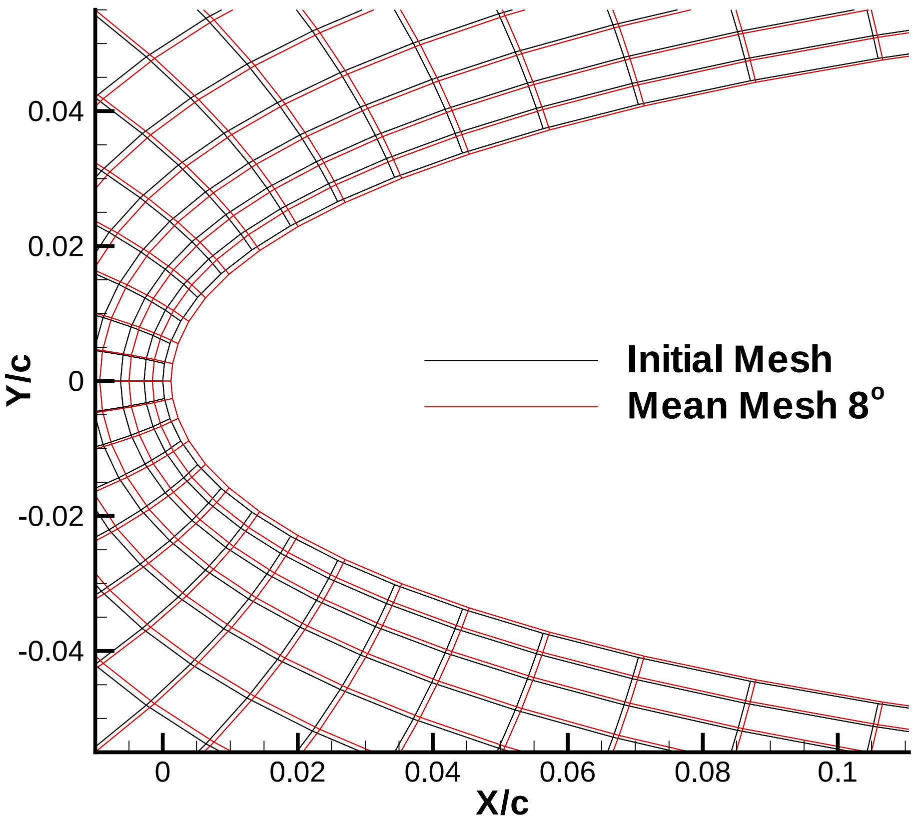

Figure 1: The Difference between the steady grid X and the mean grid $\bar{x}$ with $\alpha_0 = 8.0$

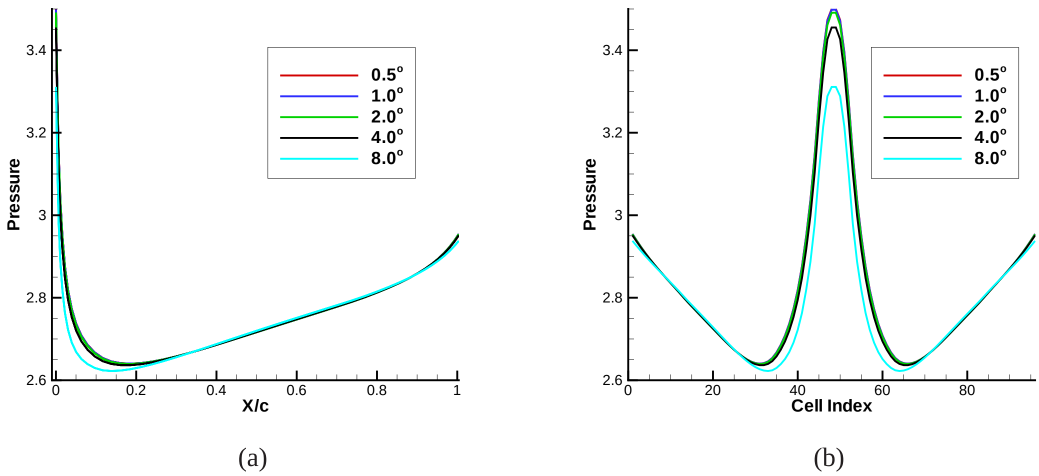

Figure 2: Mean pressure on the surface of the aerofoil and different amplitudes of oscillation. (a) plotted against chord and (b) plotted against the cell index, which starts at the trailing edge on the lower surface. First order scheme.

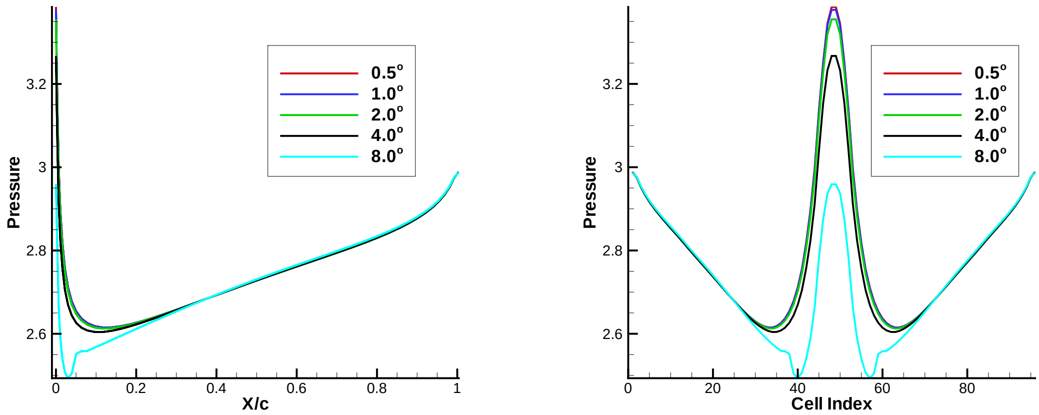

(a)

(b)

Figure 3: Mean pressure on the surface of the aerofoil and different amplitudes of oscillation. (a) plotted against chord and (b) plotted against the cell index, which starts at the trailing edge on the lower surface. Second order scheme.

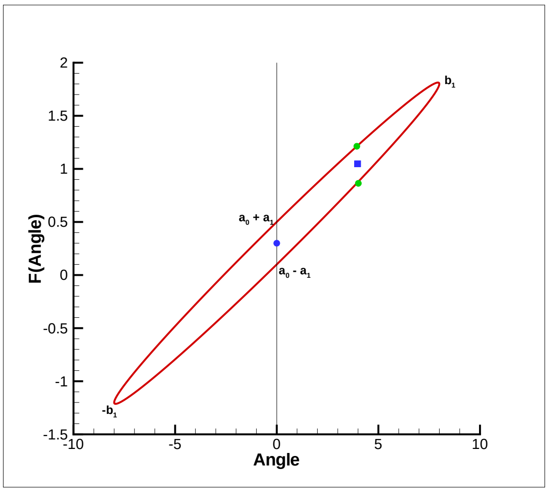

Figure 4: Schematic of one harmonic solution

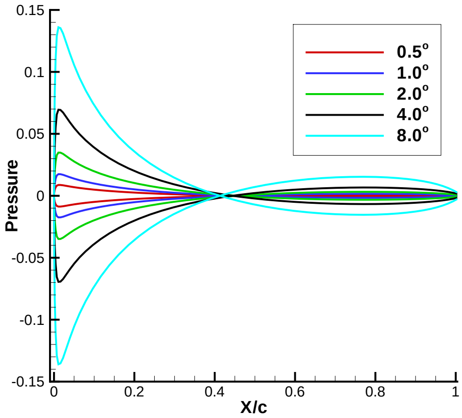

Real Un-scaled

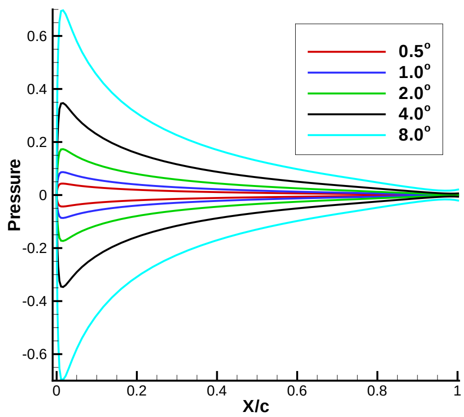

Imaginary Un-scaled

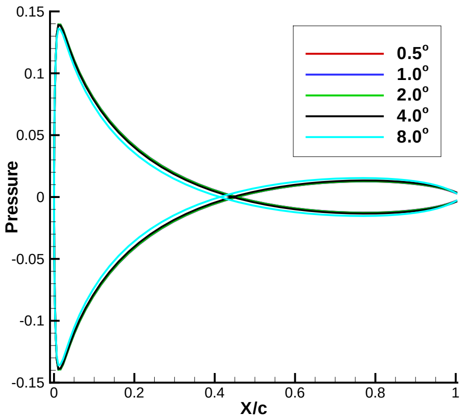

Real Scaled

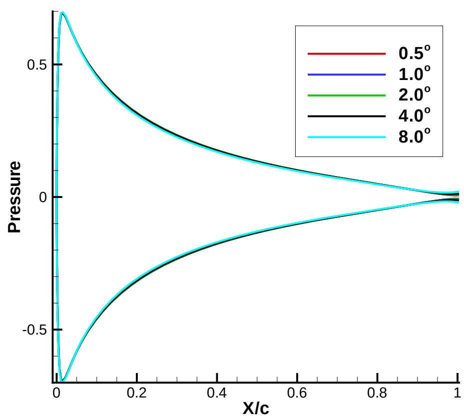

Imaginary Scaled

Figure 5: Real and imaginary parts of the pressure on the surface of the aerofoil and different amplitudes of oscillation plotted against chord for the first order spatial scheme.

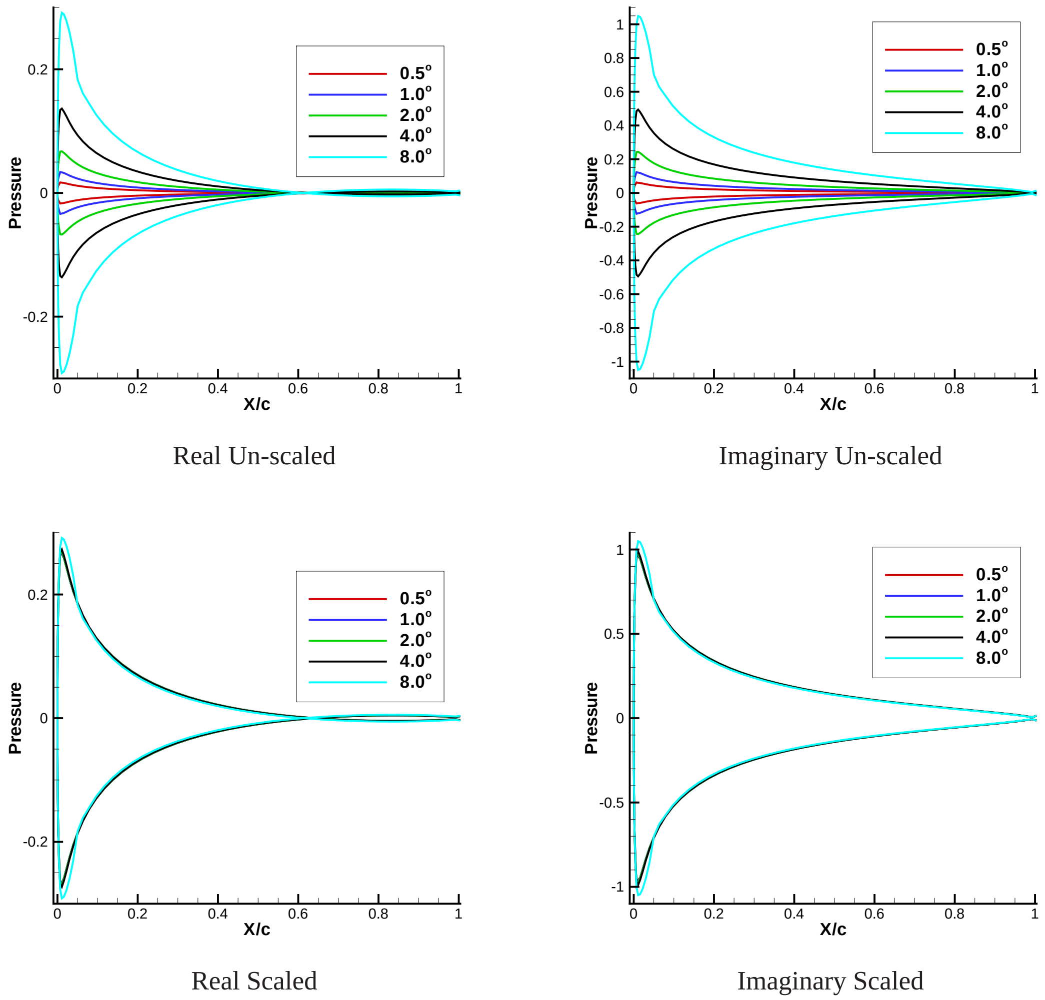

Figure 6: Real and imaginary parts of the pressure on the surface of the aerofoil and different amplitudes of oscillation plotted against chord for the second order spatial scheme.

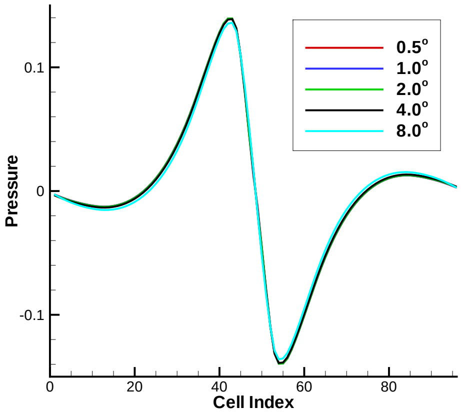

Real Scaled First Order

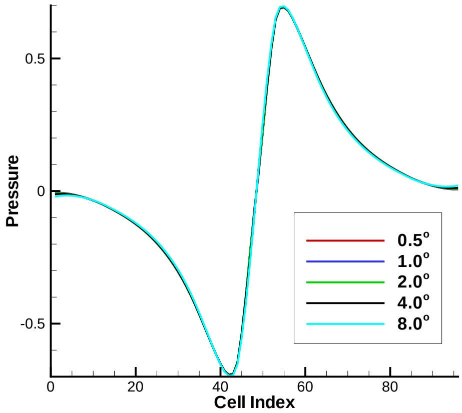

Imaginary Scaled First Order

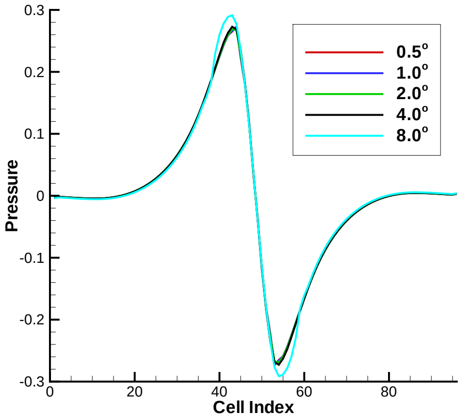

Real Scaled Second Order

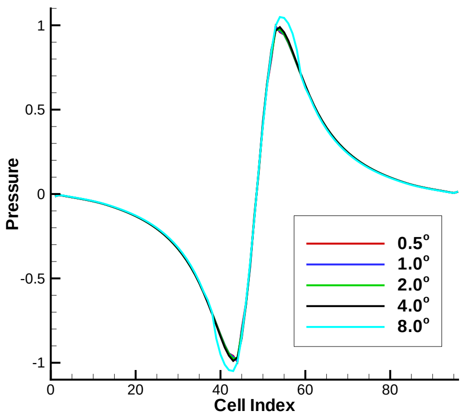

Imaginary Scaled Second Order

Figure 7: The scaled real and imaginary parts of the pressure on the surface of the aerofoil for different amplitudes of oscillation plotted against the cell index for the first and second order spatial schemes

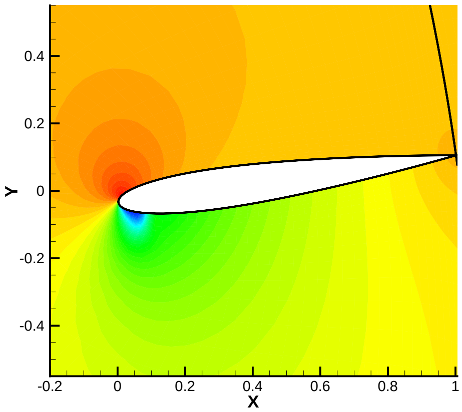

Steady Pressure Solution at 8^o down

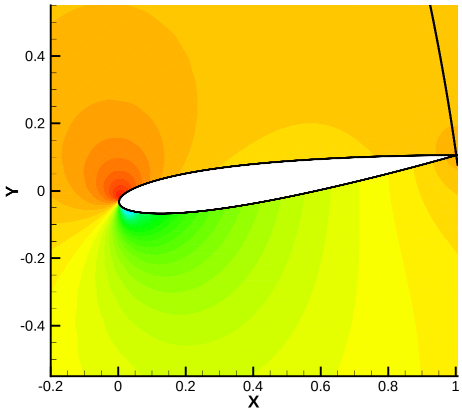

Unsteady Pressure Solution at 8^o down

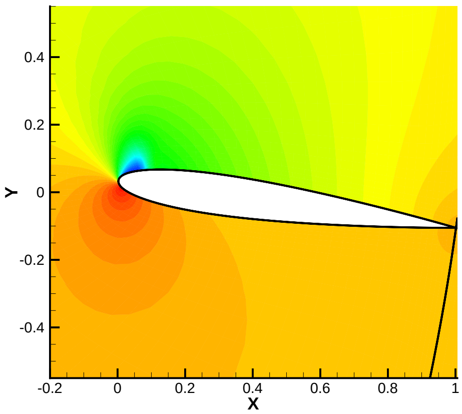

Steady Pressure Solution at 8^o up

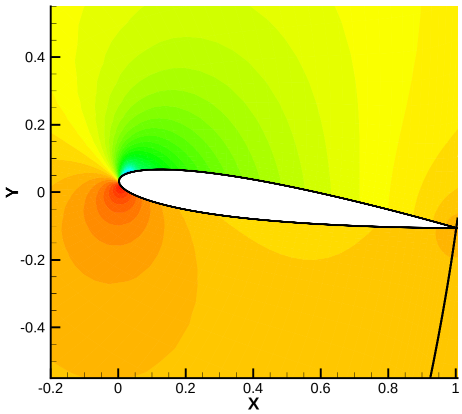

Unsteady Pressure Solution at 8^o up

Figure 8: Comparison of the steady and unsteady pressures for a free-stream Mach number of 0.5, a mean incidence $\alpha_m = 0.0$, a reduced frequency $k = 0.1$, and small amplitude of oscillation of $\alpha_0 = 8.0$ about the quarter chord.

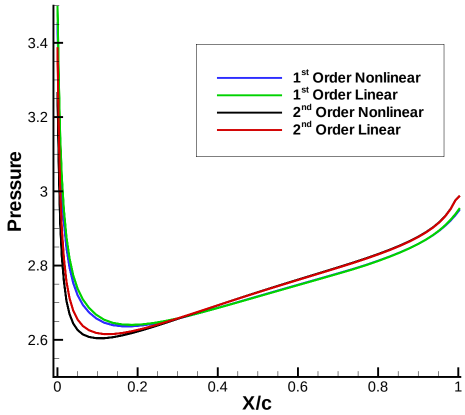

Mean pressure around the aerofoil

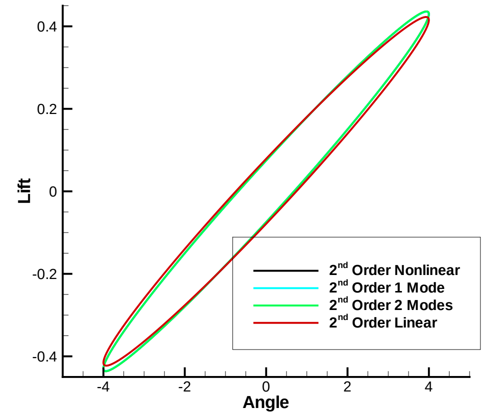

Lift curve

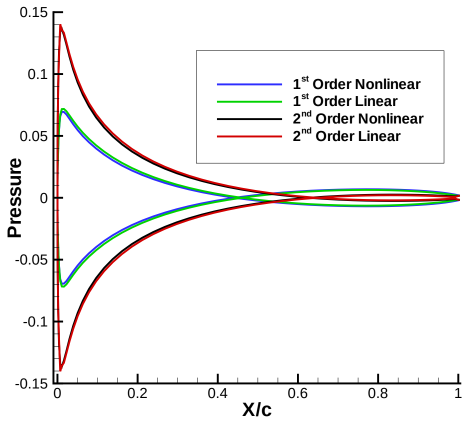

Real part of the pressure

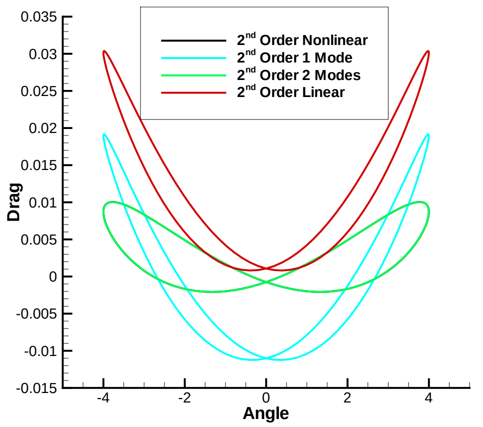

Drag curve

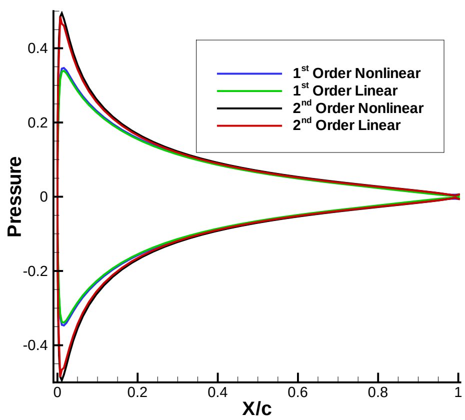

Imaginary part of the pressure

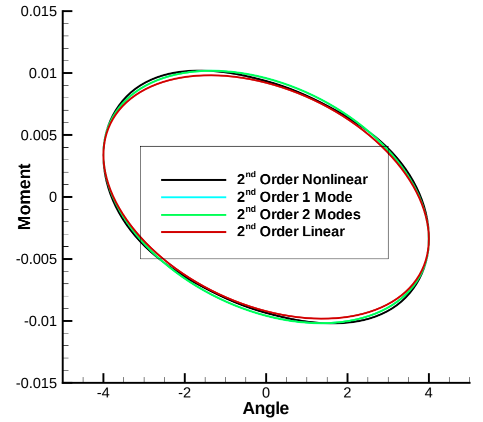

Moment curve

Figure 9: Comparison of the linear and non linear first and second order spatial schemes for test case CT0: free-stream Mach number of 0.5, a mean incidence $\alpha_m = 0.0$, a reduced frequency $k = 0.1$, and small amplitude of oscillation of $\alpha_0 = 4.0$ about the quarter chord.

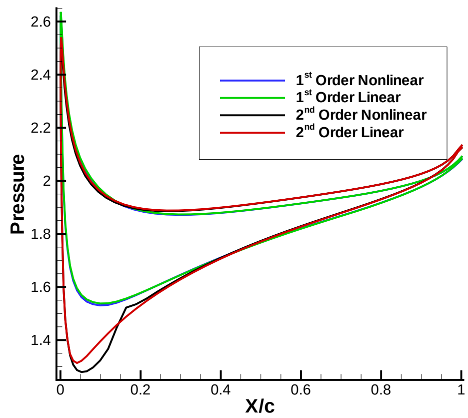

Mean pressure around the aerofoil

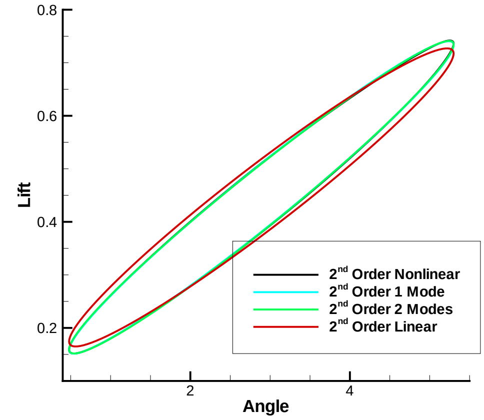

Lift curve

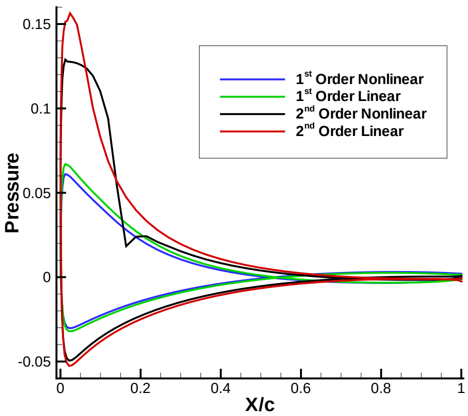

Real part of the pressure

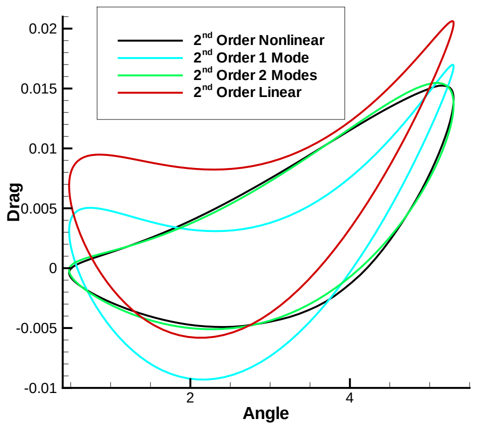

Drag curve

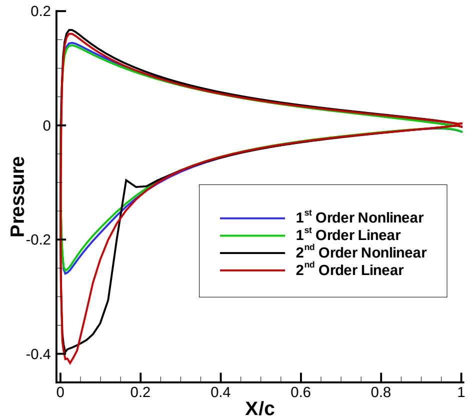

Imaginary part of the pressure

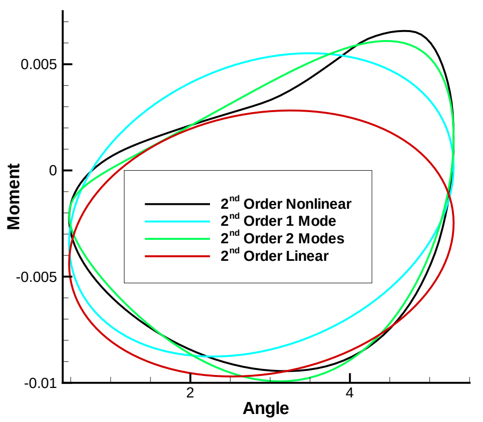

Moment curve

Figure 10: Comparison of the linear and non linear first and second order spatial schemes for test case CT1: The second test case, CT1, has a free-stream Mach number of 0.6, a mean incidence $\alpha_m = 2.89$, a reduced frequency $k = 0.0808$, and small amplitude of oscillation of $\alpha_0 = 2.41$ about the quarter chord.

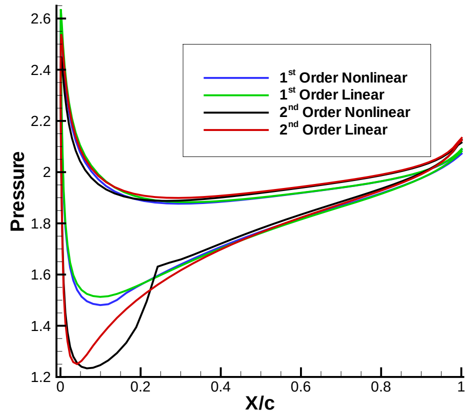

Mean pressure around the aerofoil

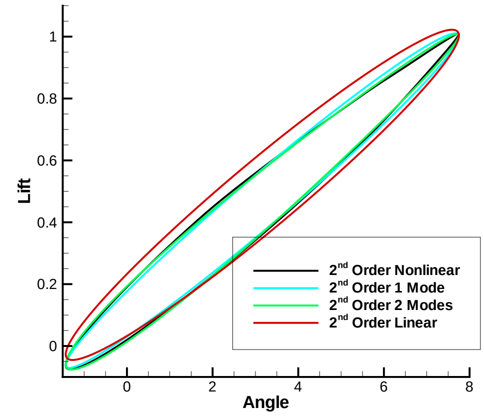

Lift curve

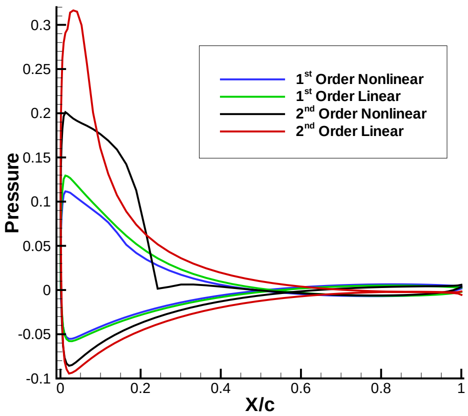

Real part of the pressure

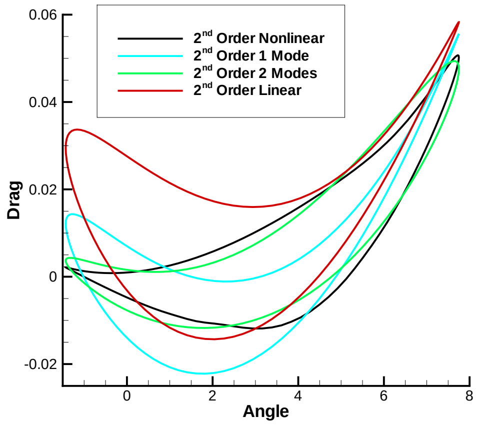

Drag curve

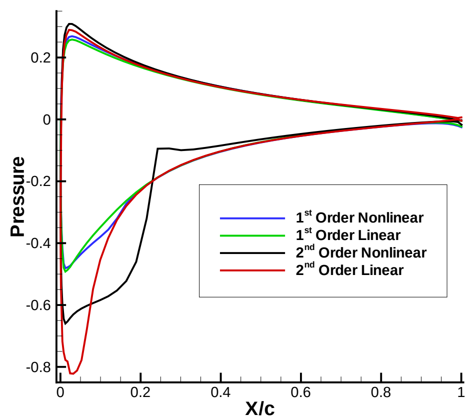

Imaginary part of the pressure

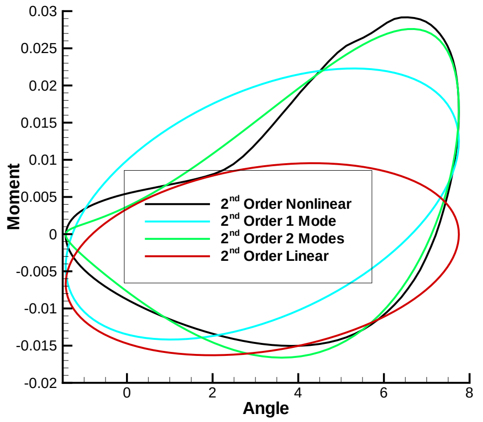

Moment curve

Figure 11: Comparison of the linear and non linear first and second order spatial schemes for test case CT2 free-stream Mach number of 0.6, a mean incidence $\alpha_m = 3.16$, a reduced frequency $k = 0.0811$, and small amplitude of oscillation of $\alpha_0 = 4.59$ about the quarter chord.

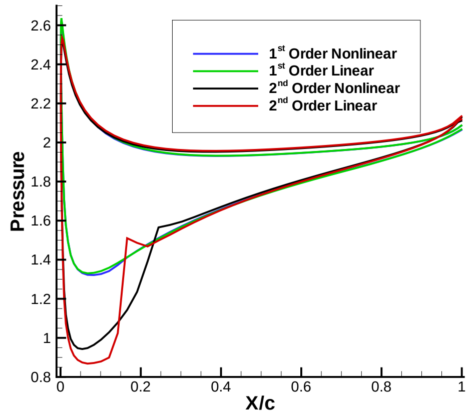

Mean pressure around the aerofoil

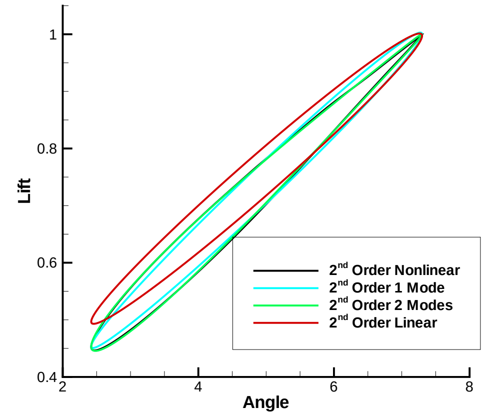

Lift curve

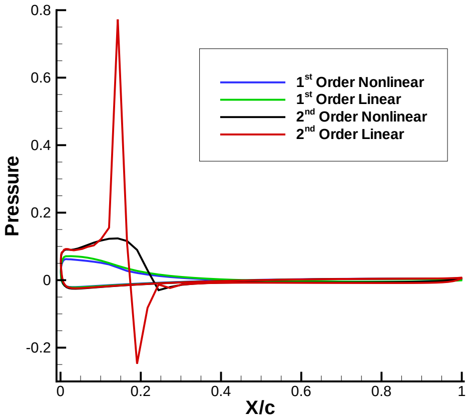

Real part of the pressure

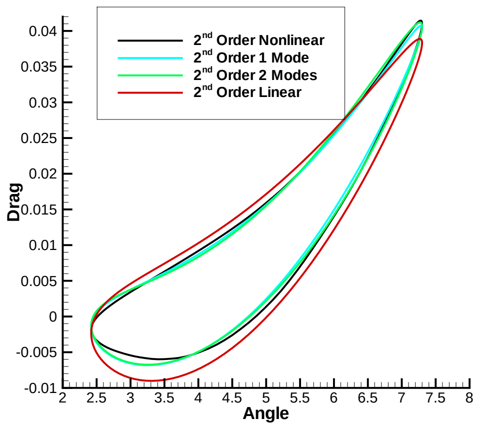

Drag curve

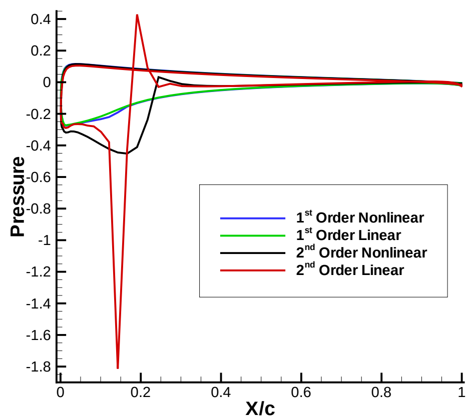

Imaginary part of the pressure

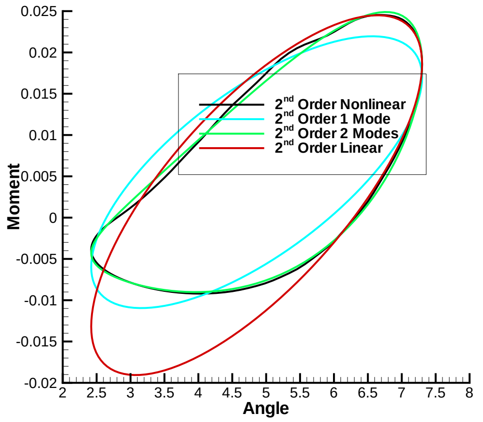

Moment curve

Figure 12: Comparison of the linear and non linear first and second order spatial schemes for test case CT3: free-stream Mach number of 0.6, a mean incidence $\alpha_m = 4.86$, a reduced frequency $k = 0.0810$, and small amplitude of oscillation of $\alpha_0 = 2.44$ about the quarter chord.

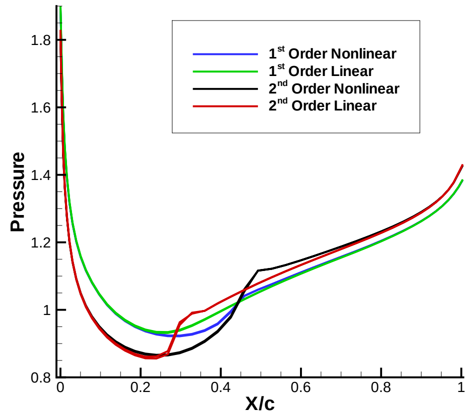

Mean pressure around the aerofoil

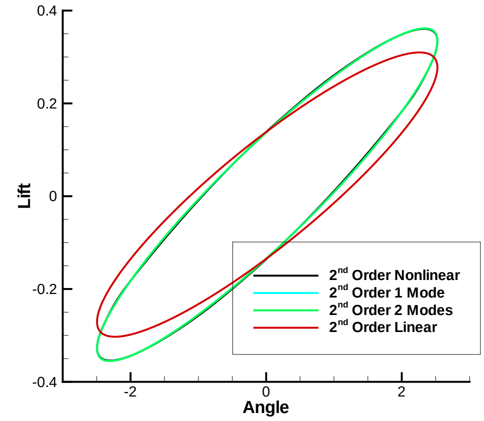

Lift curve

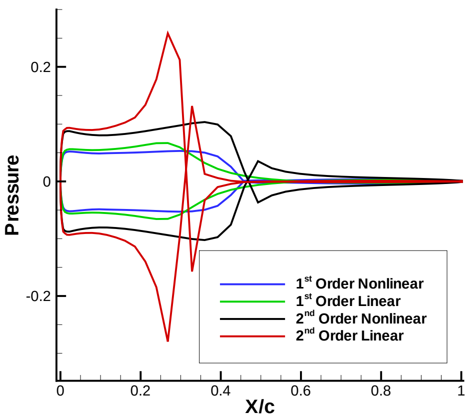

Real part of the pressure

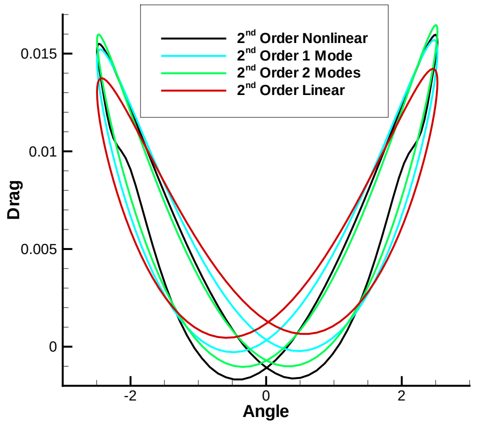

Drag curve

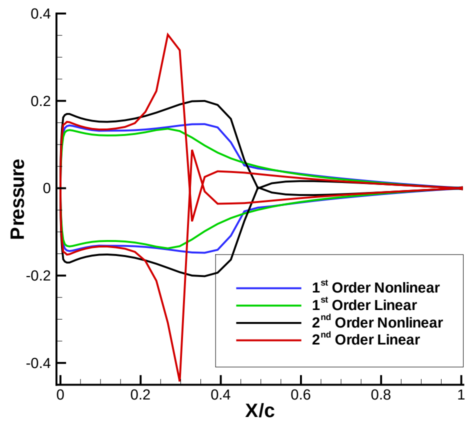

Imaginary part of the pressure

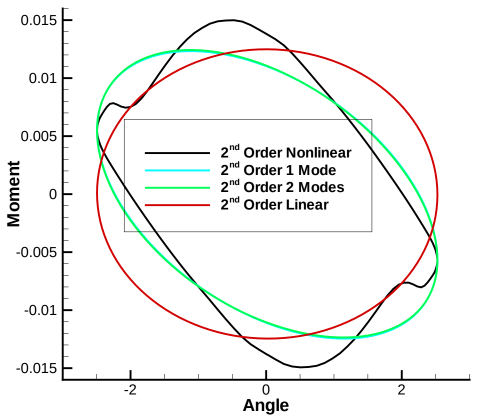

Moment curve

Figure 13: Comparison of the linear and non linear first and second order spatial schemes for test case CT5

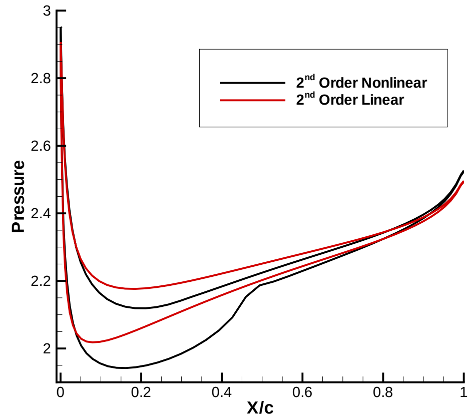

Mean pressure around the aerofoil

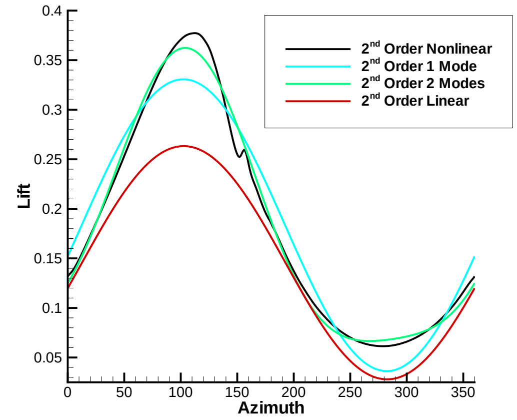

Lift curve

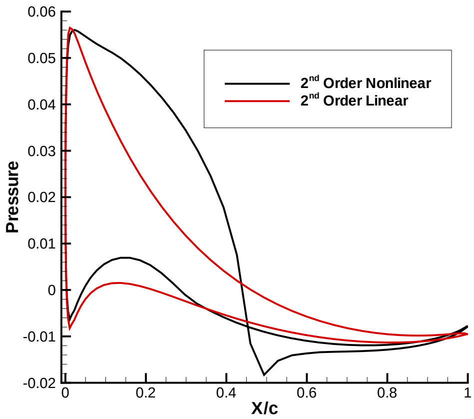

Real part of the pressure

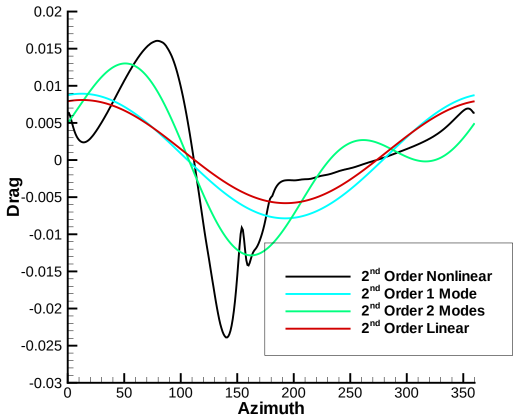

Drag curve

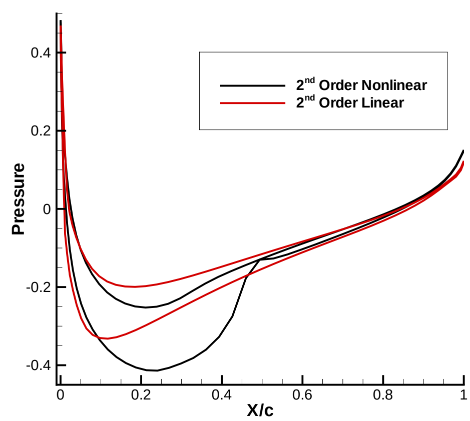

Imaginary part of the pressure

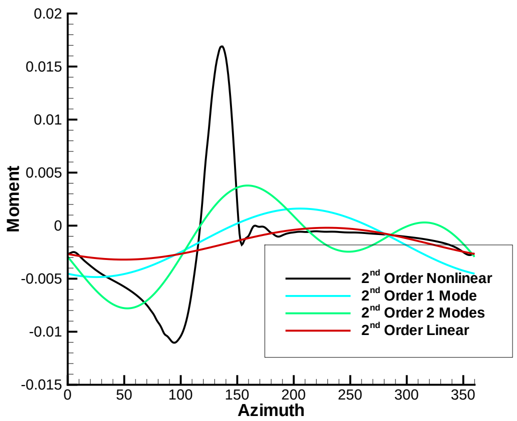

Moment curve

Figure 14: Comparison of the linear and non linear second order spatial schemes for a dMdt case

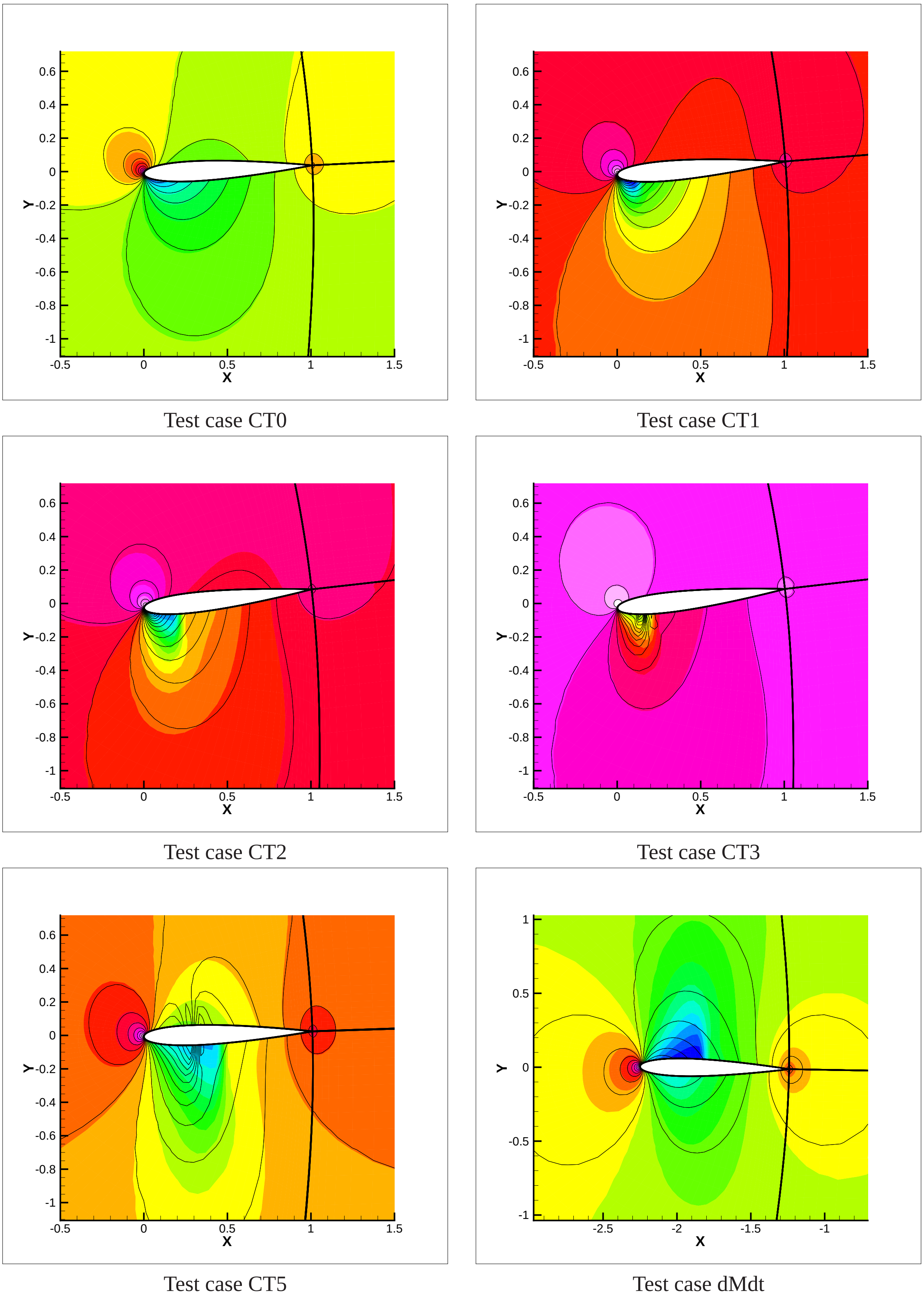

Test case CT0

Test case CT1

Test case CT2

Test case CT3

Test case CT5

Test case dMdt

Figure 15: Comparison of the non linear pressure - in colour - and the linearised pressure - black contours for the flow field around the Aerofoils

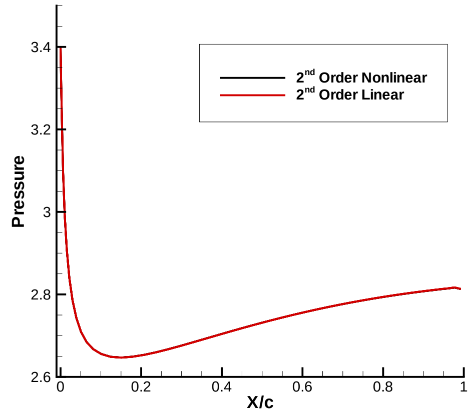

Mean pressure around the aerofoil

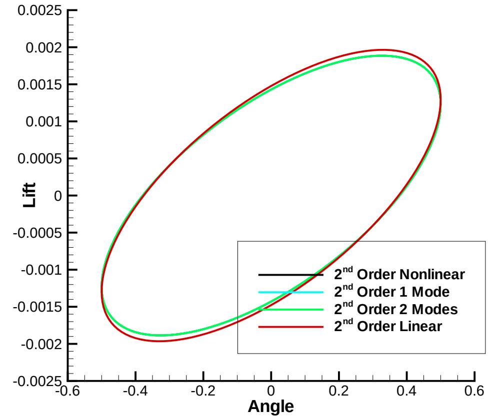

Lift curve

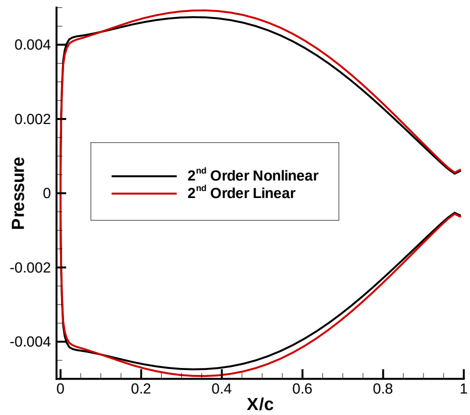

Real part of the pressure

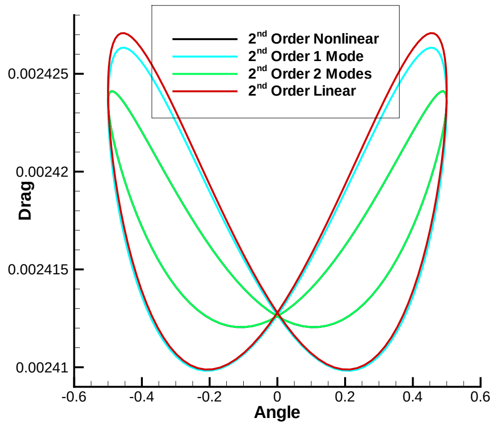

Drag curve

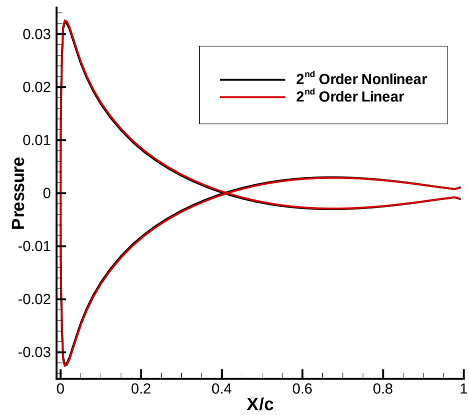

Imaginary part of the pressure

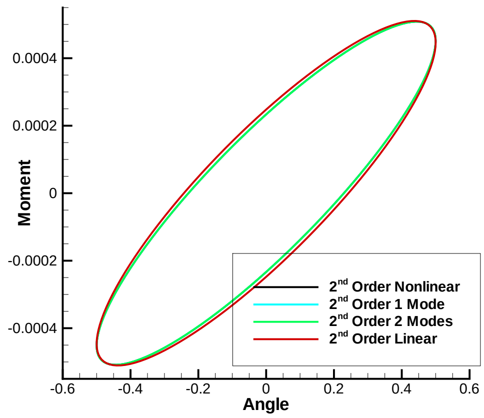

Moment curve

Figure 16: Comparison of the linear and non linear second order spatial schemes for the laminar test case $M_\infty = 0.5$, $\alpha_m = 0.0$, $k = 0.1$ and $\alpha_0 = 0.5$ about the quarter chord

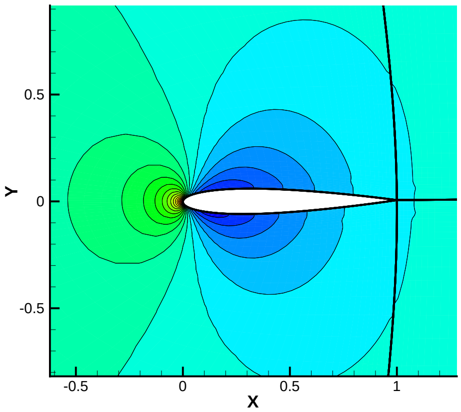

Pressure

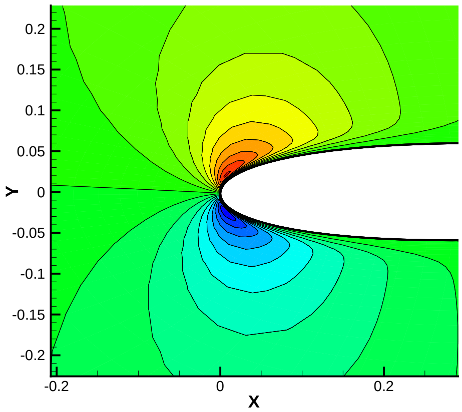

V velocity

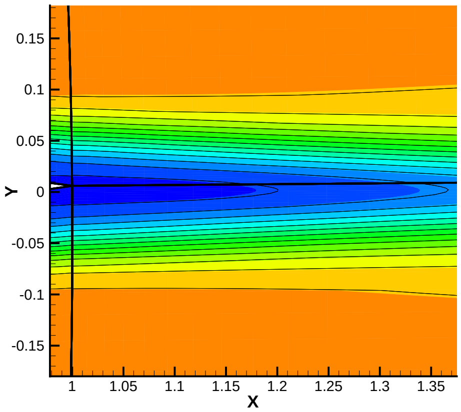

U Velocity

Figure 17: Comparison of the non linear - in colour - and the linearised pressure - black contours, flow variable for different parts of the laminar test case

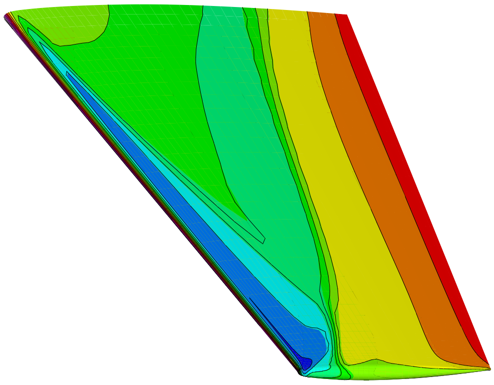

Mean pressure on the surface of the wing

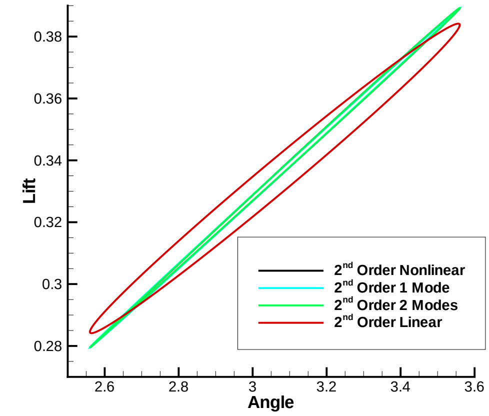

Lift curve

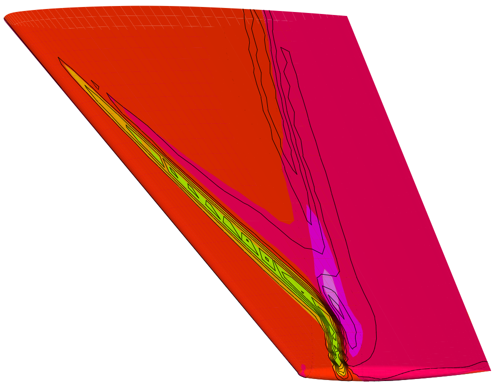

Real part of the pressure on the wing

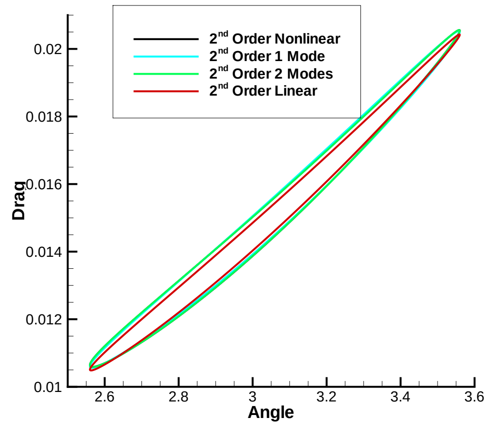

Drag curve

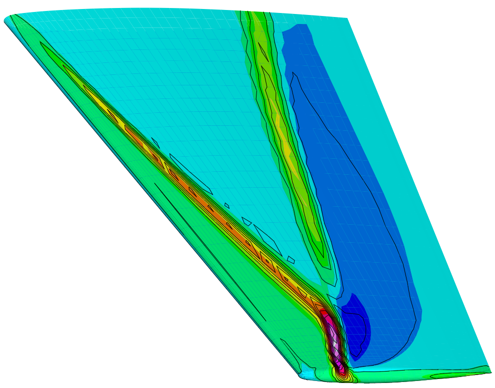

Imaginary part of the pressure on the wing

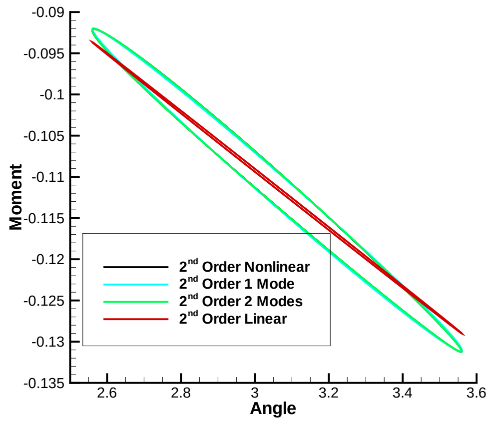

Moment curve

Figure 18: Comparison of the linear and non linear second order spatial schemes for the ONERA M6 Wing test case $M_\infty = 0.84$, $\alpha_m = 3.06$, $k = 0.1$ and $\alpha_0 = 0.5$ about the quarter chord

N_H	1	2	3	4	5	6	7
$2N_H + 1$	3	5	7	9	11	13	15
$2N_H + 1 + 2N_H(2N_H + 1)/7$	3.86	7.86	13	19.2	26.7	35.3	45

Table 1: How the 2 difference scaling are effected by the number of modes in the harmonic balance method

N_H	1	2	3	4	5	6	7
Approx cost	8	12	19	27	36	47	62

Table 2: The approximate cost of forming and solving the N_H mode harmonic balance method in terms of linear system solve of the unsteady method

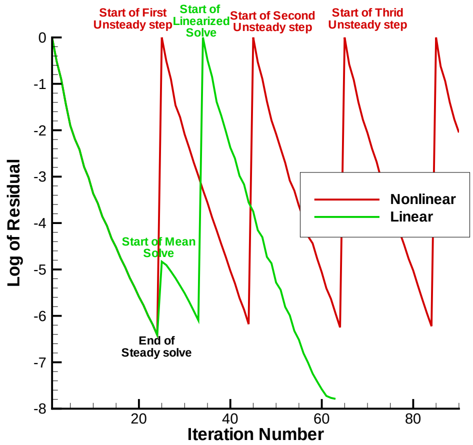

Figure 19: Comparison of the number of iterations required for the linear and non linear schemes for the dMdt test case

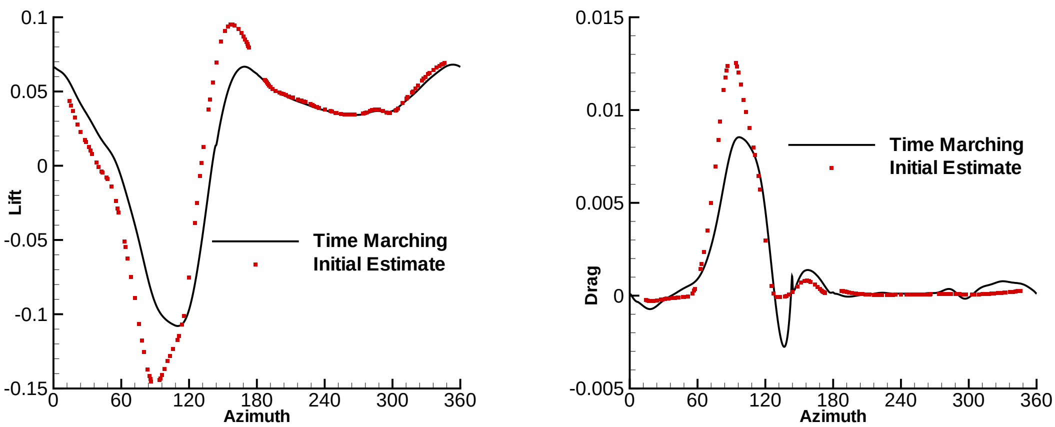

Figure 20: Initial lift and drag estimates for the dMdt test cases. The solid lines represent the time-marching solution.

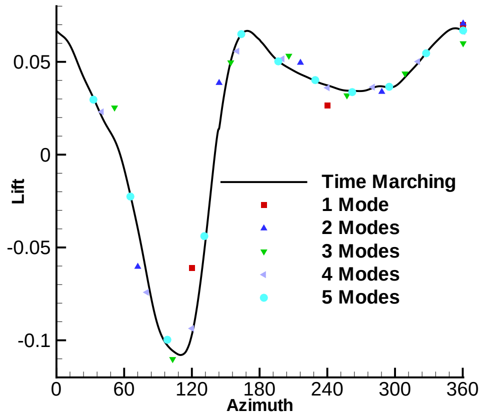

(a) Lift variation against Azimuth

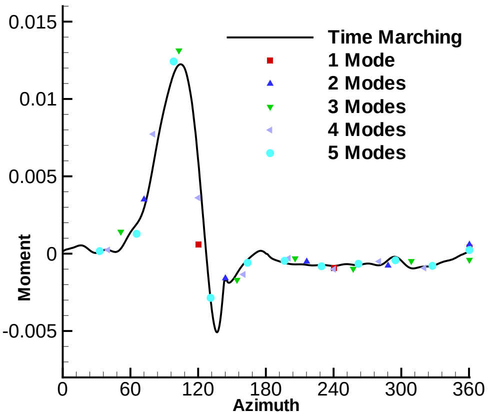

(b) Moment variation against Azimuth

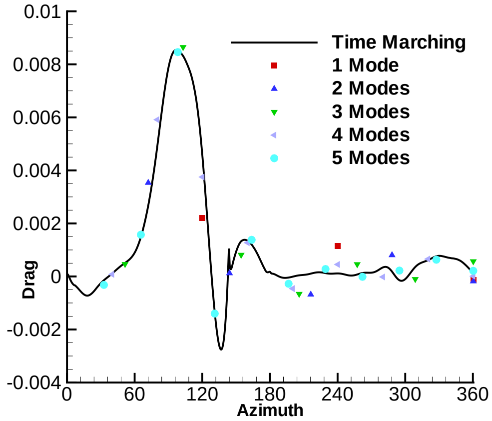

(c) Drag variation against Azimuth

Figure 21: Harmonic balance predictions for the (a) Lift, (b) Moment and (c) Drag coefficients of the dMdt case using the inviscid flow model and several modes. The solutions for the 1, 2 and 5 modes were obtained using the implicit solver while the sets for 3 and 4 modes were obtained using the explicit method.

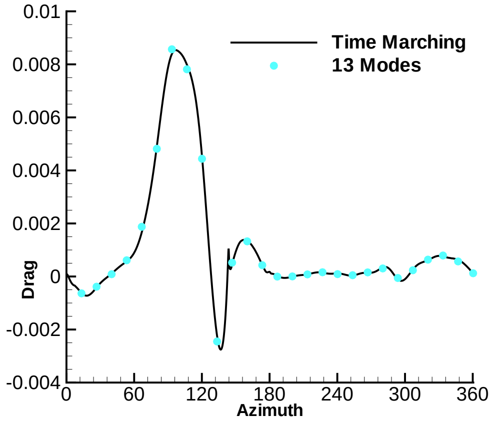

(a) Lift variation against Azimuth

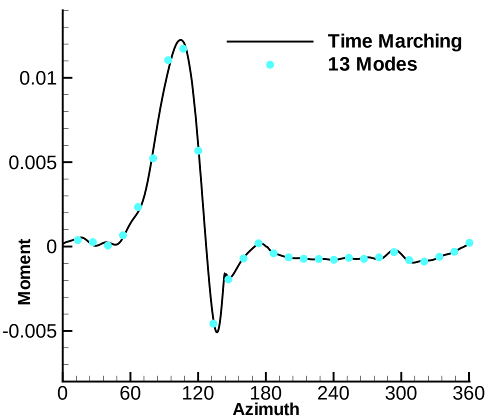

(b) Drag variation against Azimuth

Figure 22: Harmonic balance results for the lift and drag coefficients of the dMdt case using 13 modes and the inviscid flow model. The solution was obtained using the explicit flow solver.

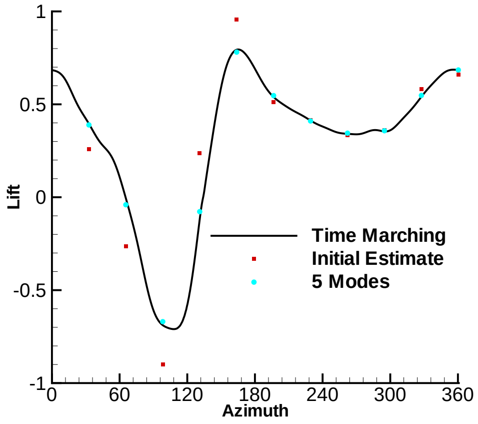

(a) Lift variation against Azimuth

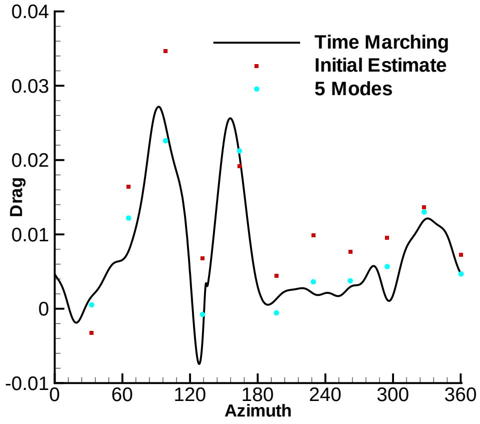

(b) Drag variation against Azimuth

Figure 23: Harmonic balance results using 5 modes for the viscous and turbulent dMdt case. The implicit flow solver was used.

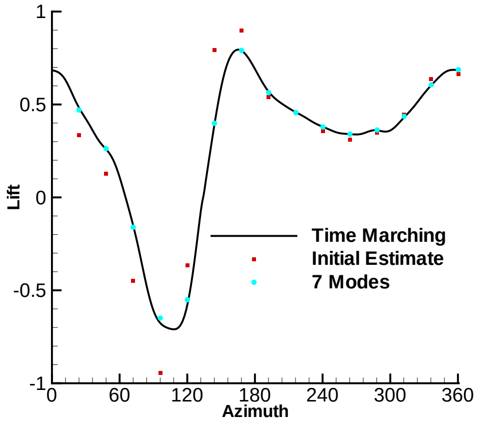

(a) Lift variation against Azimuth

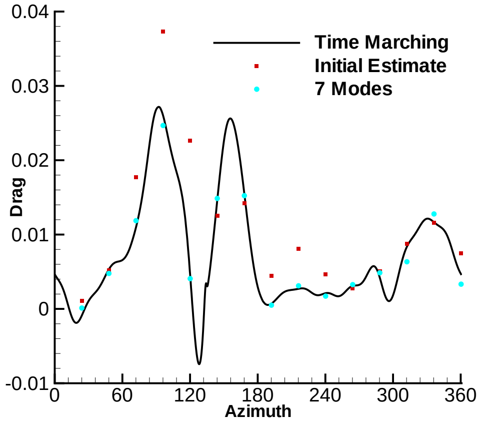

(b) Drag variation against Azimuth

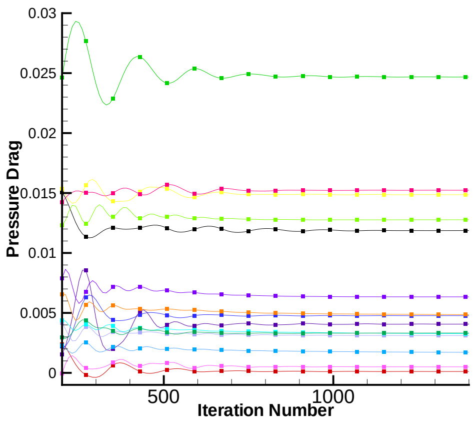

(c) Drag convergence against iteration number

Figure 24: Harmonic balance results using 7 modes for the viscous and turbulent dMdt case. The implicit flow solver was used.

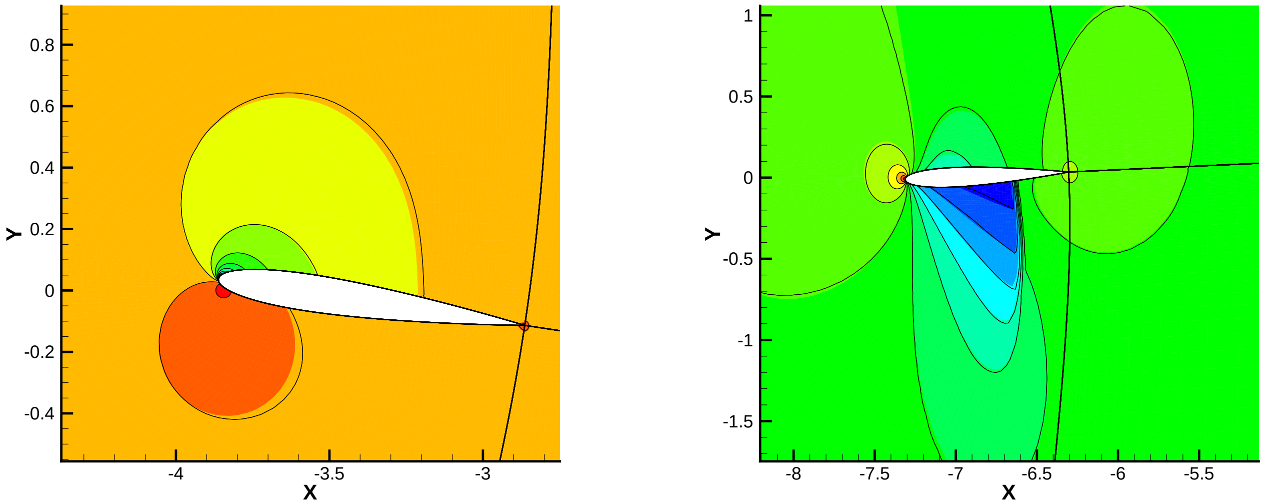

(a) Retreating side 5 modes, 295 degrees of azimuth

(b) Advancing side 5 modes, 98 degrees of azimuth

Figure 25: Harmonic balance results using 5 modes for the inviscid dMdt case. The implicit flow solver was used.

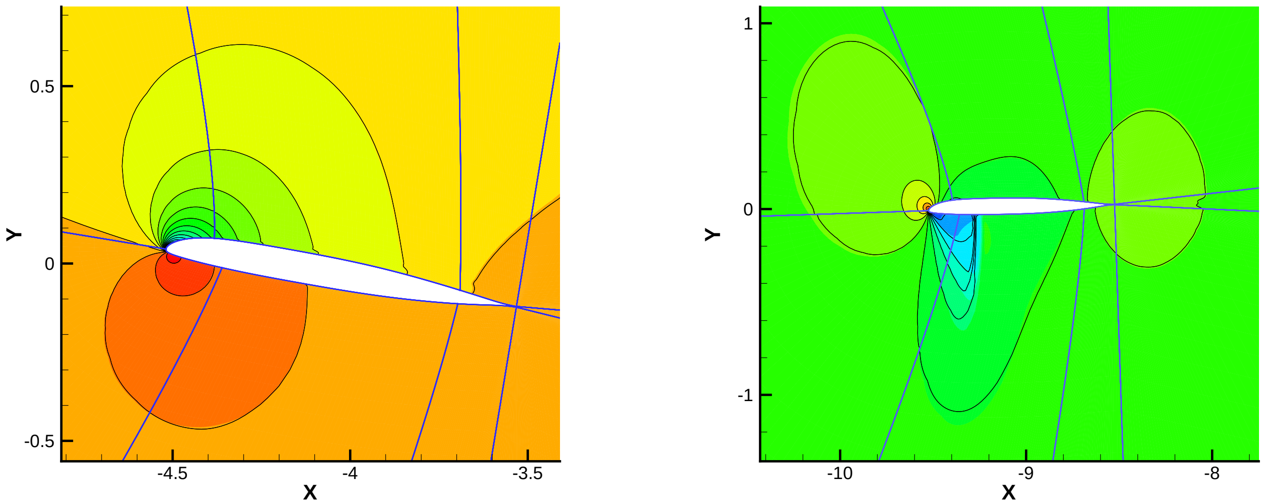

(a) Retreating side 7 modes, 288 degrees of azimuth

(b) Advancing side 7 modes, 120 degrees of azimuth

Figure 26: Harmonic balance results using 7 modes for the viscous and turbulent dMdt case using the implicit solver. The black lines correspond to the harmonic balance solution and the coloured contours to the time-marching results.

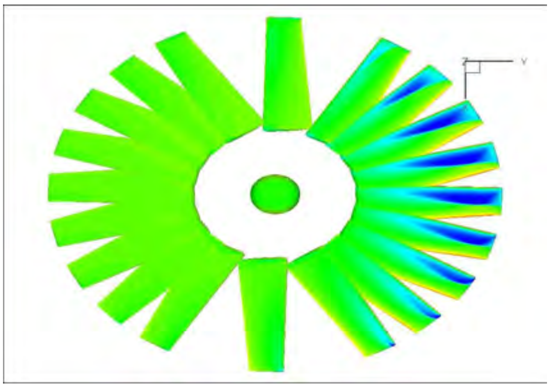

(a) Time Marching Solution

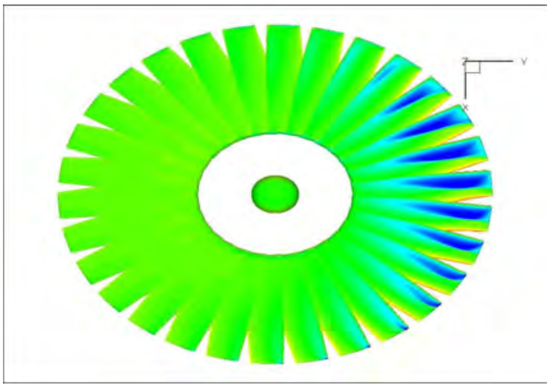

(b) Harmonic Balance Solution - 7 modes

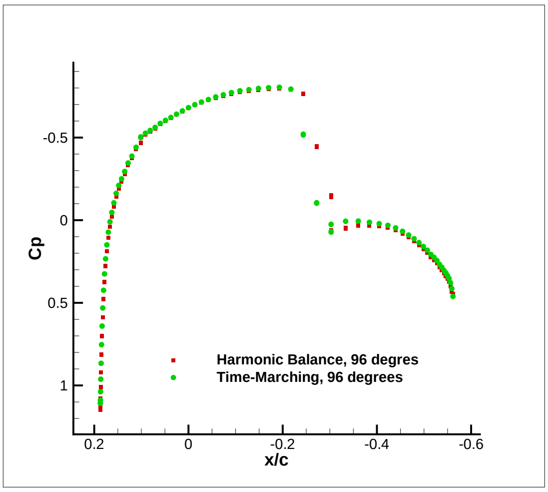

(c) 96 degrees of azimuth, r/R=0.8

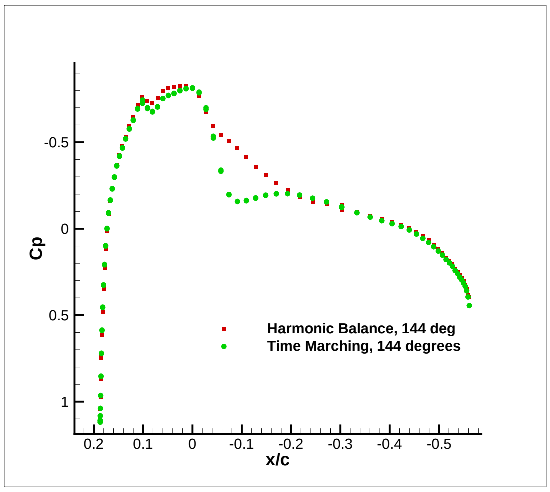

(d) 144 degrees of azimuth, r/R=0.8

Figure 27: Time Marching and Harmonic balance results for the 2-bladed ONERA non-lifting rotor in fast forward flight.